OPTICAL PROPERTIES OF Ni^{2+} AND RADIATION DEFECTS IN MgF_2 AND MnF_2

BY

LEONARD NORMAN FEUERHELM

Bachelor of Science
Oklahoma State University
Stillwater, Oklahoma
1971

Master of Science
Oklahoma State University
Stillwater, Oklahoma
1973

Submitted to the Faculty of the Graduate College
of the Oklahoma State University
in partial fulfillment of the requirements
for the Degree of
DOCTOR OF PHILOSOPHY
December, 1980

OPTICAL PROPERTIES OF Ni^{2+} AND RADIATION DEFECTS IN MgF_2 AND MnF_2

Thesis Approved:

W. A. Sibley

Thesis Advisor

J. Paul Devlin

George S. Dieke

Norman N. Durham

Dean of the Graduate College

ACKNOWLEDGMENTS

I wish to express my gratitude to the many friends who have made this study fruitful. My coworkers in the laboratory: G. Mike Renfro, Johannes Windscheif, Mark Iverson, Mike Shinn, and Dhiraj Sardar, have all endeavored to assist and inform me in the collection and analysis of this data. With them, I have learned and discussed many things besides solid state physics.

I am indebted to both the National Science Foundation and Oklahoma Christian College for financial assistance during this work. My special gratitude is extended toward Dr. Bailey McBride and Dr. James Baxter of OCC for helping to arrange a leave of absence from my duties there to work full time on this dissertation.

I appreciate more than words can express, the friendship and patient leadership extended to me over the years by my major advisor, Dr. William A. Sibley. Without his continual support and guidance, this achievement would be a mere dream without a hope of reality.

Thanks are also in order to Gary McLachlan for his kind and able assistance in the duplication of this manuscript. I also wish to thank Wendy Ward for her help with many of the drawings.

My family has endured much in this effort, and I would be remiss to think that each of them has not contributed in some way to this work. My daughter, Tessa, has sacrificed time with her father as she encouraged me to "hurry up and get your dissertation finished."

My infant son has provided motivation to achieve professional advancement with its accompanying benefits. And my loving and patient wife worked at levels well beyond the call of duty to make this dream a reality. To her go my love and admiration.

TABLE OF CONTENTS

LIST OF FIGURES

LIST OF FIGURES (Continued)

LIST OF TABLES

CHAPTER I

INTRODUCTION

Probably the most interesting aspect of condensed matter physics is the study of defects in crystals. Defects may take on many forms, and are of high interest because of the many changes they bring about in the characteristics of the crystal. Such changes affect the hardness, electrical conductivity, thermal conductivity, and optical properties such as absorption and luminesence. Defects themselves form many types, but in the study of optical properties it is the point-ion defects such as F-centers and impurities which are most significant (1). Defects may be introduced into the crystal in many ways, depending on the type of defect desired. Impurities are usually added to the melt during crystal growth (2), while radiation is used to introduce vacancies and interstitials into the crystal lattice (3). Additive coloration (4) and electrolytic coloration (5) may also be used to introduce vacancies into a crystal, but those techniques do not produce interstitials. Other techniques such as ion implantation (6) may also be used to introduce defects, with each technique having certain advantages over the other techniques.

The nature of the change caused by a defect in a crystal depends on the type of defect it is and on the crystal host it is in. For instance, in aluminum oxide, a chromium impurity imparts a dark red

color to the crystal, while a titanium impurity causes aluminum oxide to appear blue (7). In this case the host material is the same, but different impurities produce optical absorptions of different energies of light, accounting for the varied colors. Similarly, radiation damage by electron bombardment produces F-centers in most crystals, but the resulting effects of such defects vary from host to host. In KCl, the F-center causes the crystal to change from transparent to deep blue in color. In MgF_2, the F-center has its absorption in the UV-region, and only very minor changes in coloration are noticeable. So the same defect causes different effects in different host materials.

These various defects have become important to us technologically in the past few years (1). Starting with the ruby laser (Cr^{3+} in Al_2O_3) (7), defects in crystals are employed in ways such as tunable, solid state lasers (F-center laser) (8), information storage systems (9) and hardened window materials for lasers (10). Especially in the area of tunable lasers, and in the field of up-conversion (11,12), defects in crystals seem to hold the key to the devices of the future.

Consequently, much work has been done by numerous researchers in characterizing the effects of impurities and radiation-induced defects in crystals. The earliest work was done on the simplest crystals, namely alkali halides. It was the simplicity of this crystal structure that allowed the positive identification of radiation induced defects such as the F-center and F-aggregate centers in terms of ion vacancies. DeBoer's work (13) defining the F-center to be a negative ion vacancy with an electron for electrical balance, and Van Doorn's (14) outstanding paper showing the M-center and R-center to be clusters of two and three F-centers, were a milestone in

understanding radiation effects. Other review articles have summarized the extensive work done in alkali halides (15-19).

Duncanson and Stevenson (20) were among the first to look at MgF_2. This material is normally transparent from 1100 A to about 15μm, as indicated in Figure 1. Because of this wide range of transparency, it is optically desirable as a window material, or for use as a thin film coating to reduce reflections. MgF_2 is a rutile-structured material, as Figure 2 shows. This figure displays two unit cells of MgF_2, and shows the relavtive positions of the fluorine atoms to the magnesium atoms. In the crystal, the a and b lengths are identical, being 4.623 A, with the c length being shorter, 3.052 A. This gives the crystal an overall symmetry of D_{2h}. This is a somewhat lower symmetry than the O_h symmetry found in cubic crystals.

Various researchers have studied the effects of radiation on pure MgF_2. Hills and McBride (21) suggested that absorption bands at 260 nm and 370 nm should be identified with F and M (or F_2) centers, respectively. Blunt and Cohen (22) reaffirmed these assignments and further tentatively identified the 370 nm absorption band as arising from the F_2 center having C_{2h} symmetry in the crystal. They also made tentative assignmentof the 320 nm absorption band to the F_2 (D_{2h}) center.

Facey and Sibley (23-25) went on to study the growth of these bands with radiation dosage, the effect of bleaching, and to connect luminescence bands with the various absorption bands. The 370 nm absorption band was found to luminesce at about 420 nm, and the F-center, if other centers were absent, emitted a luminescence at about 430 nm. Another band with absorption at 400 nm and luminescence

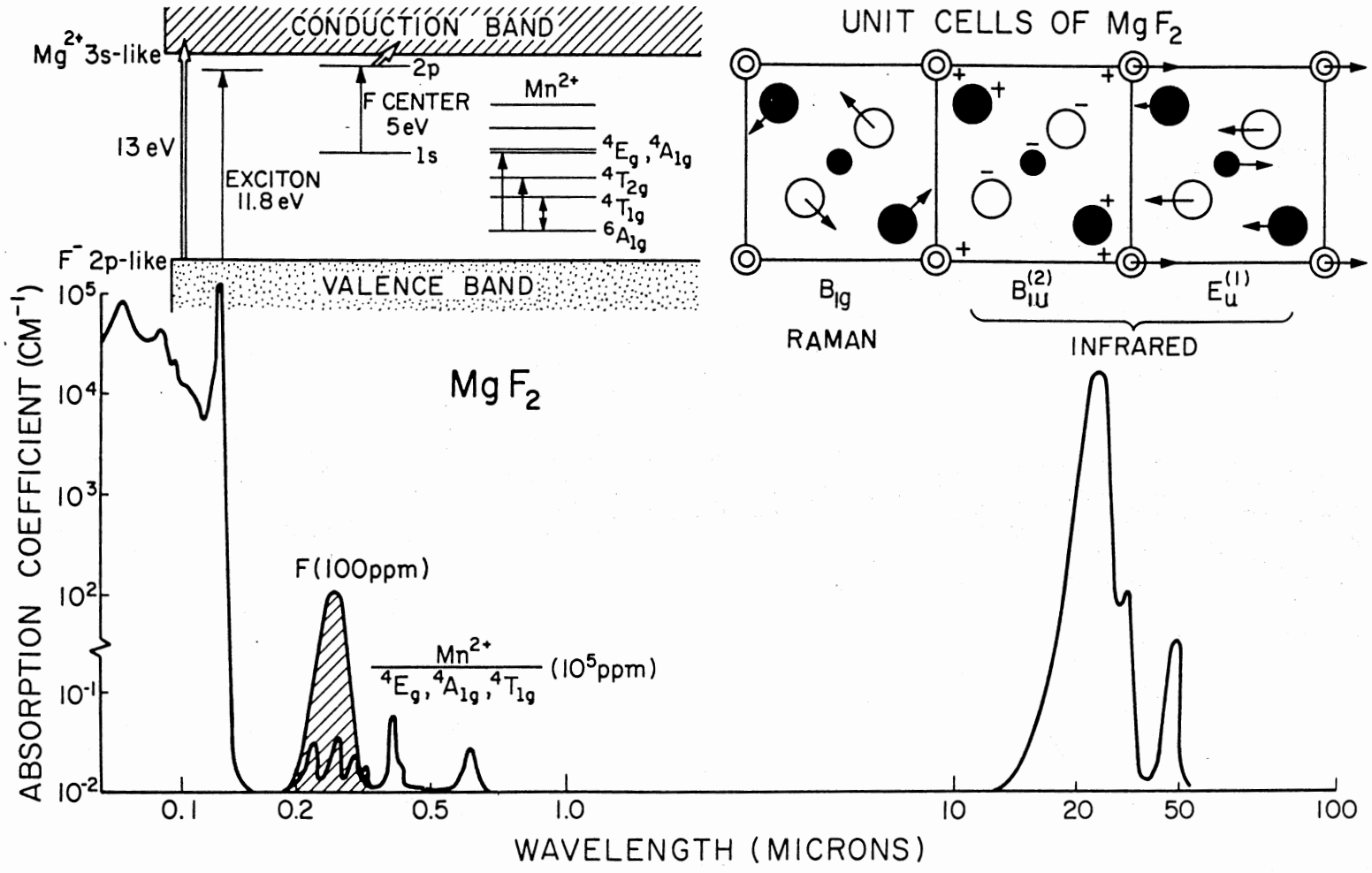

Figure 1: The Optical Properties of MgF_2

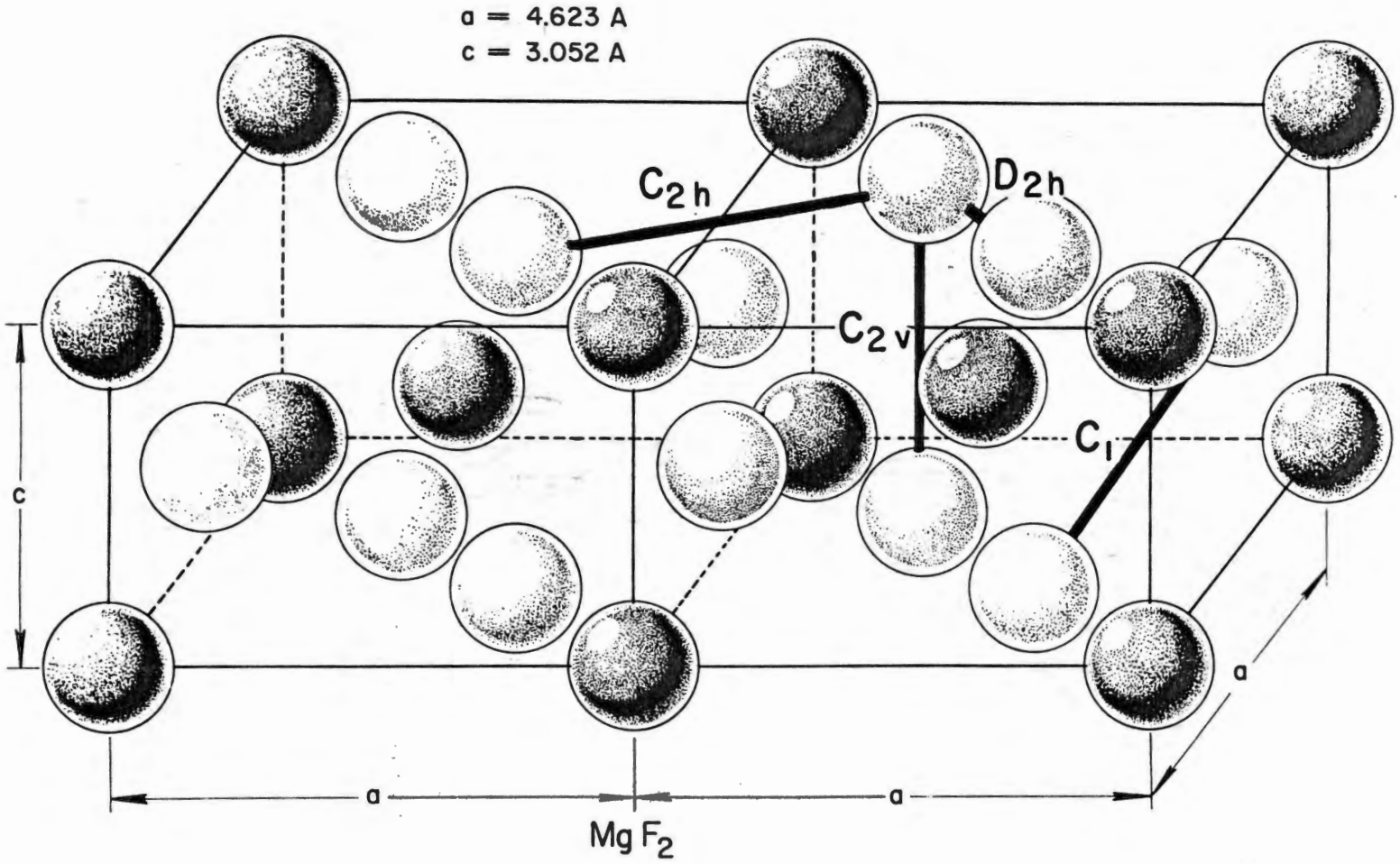

Figure 2: Two Unit Cells for MgF_2

at 600 nm was noted, and because this band was unpolarized, was identified as probably arising from the F_2 (C_1) center.

Study of the figure of the two unit cells of MgF_2 indicates that four possible orientations of the F_2 center exist, each different type being identified by its symmetry in the crystal. One expects that the defects may be identified by the polarization of the absorption and emission of each type of center, as follows. Two of the centers have major dipoles that are essentially perpendicular to the C-axis of the crystal. These are the F_2 (C_{2h}) and F_2 (D_{2h}) centers. One expects that these defects will be strongly polarized $E \perp C$, with only very weak, if at all measurable, components that are $E \parallel C$. However, the F_2 (C_{2v}) center has its dipole in the C-axis direction, and would be expected to be strongly polarized $E \parallel C$. The fourth type of F_2-center has 16 possible orientations within the crystal, and is not expected to show any preference of polarization. Thus the F_2 (C_1) center should be unpolarized. Likewise, the F_3-center would have dipoles in directions both parallel and perpendicular to the C-axis, and should be unpolarized.

Attempts to fit the experimental data to various models have met with reasonable success for these defects. Mostoller and his co-workers (26) used the one-phonon density of states model proposed by Mostoller, Ganguly, and Wood (27) to fit the F_2 (C_{2h}) absorption and luminescence data with vibronic structure information found at low temperature. However, most defect centers lack the wealth of vibronic structure that this particular center has. Other models involve the configuration coordinate model (28,29) for fitting absorption and emission spectra in terms of some dominant phonon mode

in the crystal. This will be discussed more fully in chapter two. Also used for the F-aggregate centers is the hydrogen molecular ion model, initially used by Aegerter and Luty (30) to explain F_2^+-centers in KCl. Applied to F-aggregate centers, basically the F_2-center can be treated as an H_3 molecular complex, and F_2^+-and F_3^+-centers as ions of these. Using the work of Herman et al. (31), Mulliken (32), Slater (33), Present (34), Bates et al. (35), Coulson (36), and James and Coolidge (37), one can predict a defect center absorption energy from the distance between the vacancies in the defect complex (38). While this approach is admittedly not as sophisticated as the other models, it appears to give reasonable agreement with the experiment, and helps to separate the numerous bands that appear in irradiated MgF_2. We shall see more of this model in chapter four.

As has been mentioned before, impurities also form important point-ion defects. In the rutile materials of MgF_2 and MnF_2, numerous researchers (39-46) have examined the effect of impurities on the absorption and luminescence of these crystals. Blunt (39) and Johnson et al. (40), were some of the earlier workers in this field. In recent times, Moulton and Mooradian (47) have been interested in the nickel-doped MgF_2 crystal as an infrared laser material, and have studied the temperature dependence of this crystal. Iverson and Sibley (48) have looked at the nickel impurity in a variety of host crystals, as did Vehse et al. (49). The rationale for examining several host materials, especially those with slightly different crystalline structures, is that the energy levels of the impurity ion change only slightly with different crystals, and studying several together often gives a more complete picture of the

impurity's effects. Further, some of the hosts would have simpler crystal symmetry than does the rutile structure, allowing for a more straightforward analysis of the effects seen experimentally.

In particular, the analysis of an impurity being in a site have cubic O_h symmetry is usually simpler than if the site symmetry is of lower symmetry. Comparison is often made, then, of MgF_2 with $KMgF_3$ or similar crystals which have cubic perovskite structure and thus a higher site symmetry. Comparion is sometimes also made with a crystal such as MgO, although the oxide is often significantly different in certain of its characteristics. Likewise, comparison of MnF_2 with $KMnF_3$ is common, and energy level comparisons are reasonably close, although the splittings do change because of the different site symmetries.

One thing that should be pointed out here is that the different site symmetry of the impurity changes the group theory nomenclature for that energy level. For instance, what is the $^3T_2$ level of Ni^{2+} in O_h symmetry splits into $^3B_2 + {}^3A + {}^3B_3$ levels in the D_{2h} symmetry of MgF_2 (49). However, to facilitate comparison with the more common O_h symmetry levels, and to keep the nomenclature a little simpler in this paper, the O_h terminology will be used instead of the more correct (and confusing) D_{2h} terminology. Readers are referred to Cotton (50) for a more detailed explanation of the differences in nomenclature.

Thus, in this paper will be a theoretical look at the energy levels of defects, and in particular impurity ion defects, in crystals, with a look at fitting the temperature dependence using a quantum mechanical single configuration coordinate model developed by Struck

and Fonger (51-55). Energy transfer processes are also examined briefly. The discussion and analysis of experimental work is divided into two parts. The first part examines radiation defects in pure MgF_2, with special emphasis on the identity of the absorption bands of the F_3-center and the F_2 (C_1) and F_2 (D_{2h})-centers. Then the nickel-doped crystals of MgF_2 and MnF_2 are studied, including an analysis of the temperature dependence of the various luminescence transitions, analysis of energy transfer processes between the Mn^{2+} ions and the Ni^{2+} ions, and finally a look at radiation damage in these crystals.

CHAPTER II

THEORETICAL BACKGROUND

Let us consider first the theory of the absorption and emission of light in a crystal, with special emphasis on the role played by radiation defects and by impurity ions. The configuration coordinate model will be introduced as a tool for dealing with electron-phonon interactions, and various computational schemes for dealing with the configuration coordinate model will be examined. Finally, we will look at energy transfer in these crystals.

Absorption and Emission of Photons

The basic approach to absorption in an insulator is to assume that a localized point defect or ion in the crystal is excited to some higher energy state by the incident photon. That only certain energies of incident light are absorbed is due to the idea that certain discrete energy levels exist for the ion or defect. We find the energy levels by solving Schrodinger's equation using the following Hamiltonian (56):

$$H = \frac{-\hbar^2}{2m} \sum_i \nabla_i^2 \; - \sum_i \frac{Ze^2}{r_i} \; + \sum_{i>j} \frac{e^2}{r_{ij}} + \sum_i C\,(r_i)\bar{\ell}_i \cdot \bar{s}_i + H_c \qquad (1)$$

These terms describe the kinetic energy of the electron, the

electrostatic interaction between the nucleus of charge Ze and the electrons, the electrstatic repulsion between electrons, the spin-orbit interaction, and the crystal field interaction, respectively. The sums run over the number of electrons bound to the ion. The vector $\vec{r}_i$ is the vector from the nucleus of the ith electron, while r_{ij} is the vector between the ith and jth electrons, or $|r_i - r_j|$. The first four terms could be considered the free ion Hamiltonian, while the H_c term accounts for the interactions of the ion with the surrounding lattice ions.

In order to evaluate the Hamiltonian, both the symmetry of the crystalline field, and also something of the relative magnitudes of the interaction terms must be known. The typical assumption (also the simplest) is to assume an octahedral crystal field symmetry. For many crystals this is exactly the situation, and for others, it is a reasonable approximation. Two general cases are then assumed, one being that the crystal field energy is small compared to the interelectron repulsion energy. This would have the Hamiltonian fairly close to the free ion Hamiltonian, and is known as weak field coupling. The second case, called the strong field case, is when the term H_c is much larger than the interelectron repulsion, and thus the energy levels are very different than for the free ion.

For the transition metal ions, Tanabe and Sugano worked out the energy levels for the strong field case of octahedral symmetry. The diagram for Nickel^{2+} and Cobalt^{2+} are shown in Figure 3. In Figure 3, for Ni^{2+}, we see that at the left side the 3-d electrons have been coupled together to form various ^{2S+1}L terms. For these terms, Σr_{ij}^{-1} is diagonal, and the matrix elements of H_c are found between

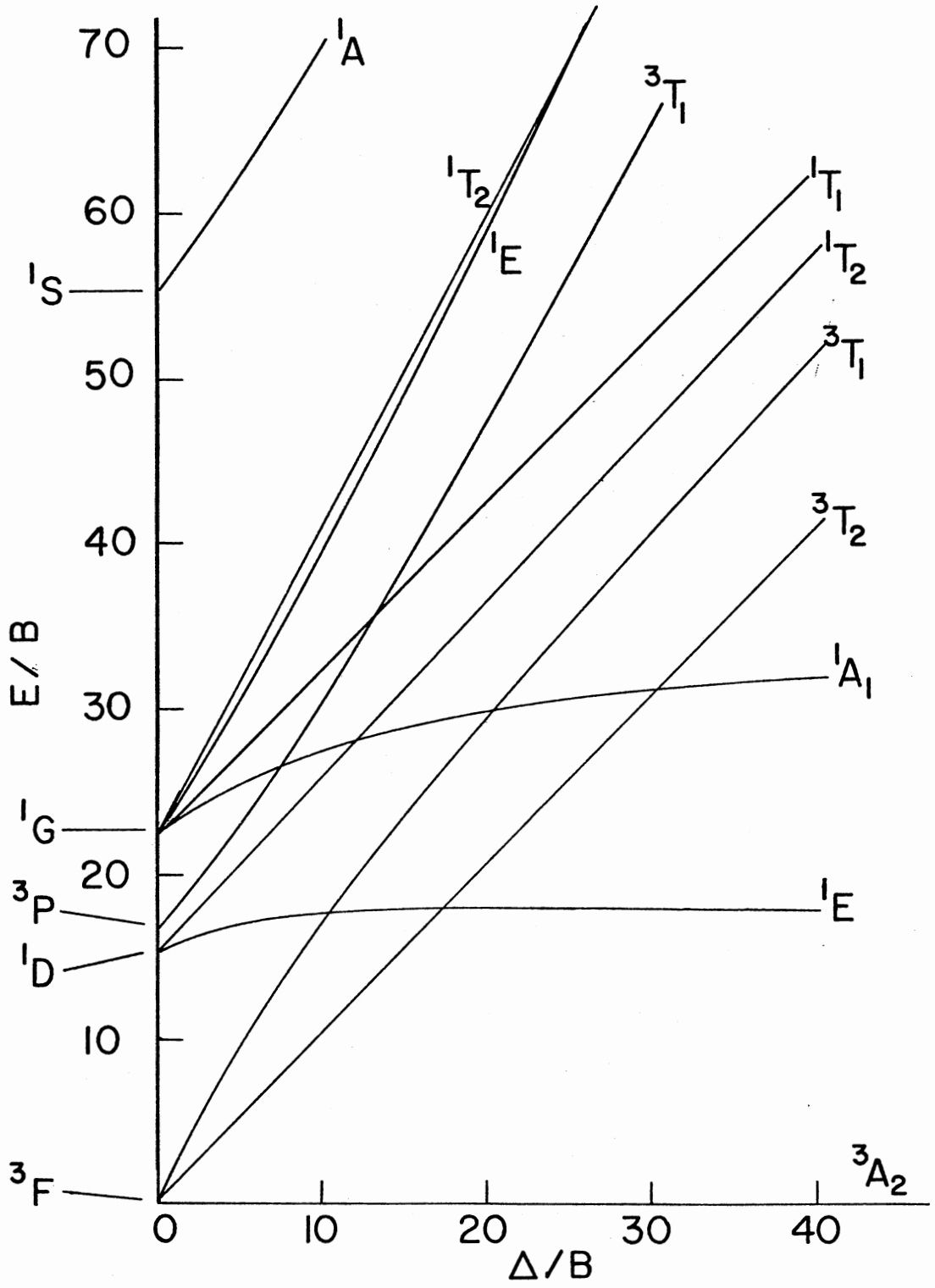

Figure 3: Tanabe-Sugano Diagram for Ni^{2+}

these states. The other extreme is toward the right side of the diagram, where the configuration diagonalize H_c. The result of this is terms of the form $^{2S+1}\Gamma$, where Γ is the group theory symbol for the symmetry of the level.

The spin-orbit term should be mentioned here as well, because the effect of it is to reduce the degeneracy of the energy levels. For 3-d ions, the spin-orbit spitting is generally small compared to the crystal field effect, so that the most noticeable effect is to cause splitting of the zero phonon lines for various transitions. Further, the lifting of the degeneracy of the levels allows a means of determining if certain transitions are electric dipole or magnetic dipole. This knowledge often allows us to determine which of the spin-orbitsplit levels is the lowest.

Configuration Coordinate Model

Experimentally, it is observed that absorption and emission bands for 3-d ions, even though they are transitions from one discrete energy level to another, are not sharp lines but rather are broadened out in gaussian type bands which center on some peak energy. The model most generally used to explain this is the single configuration coordinate (SCC) model outlined by Fitchen (28), Klick and Schulman (29) Fowler (18), Dexter (58), and DiBartolo (59). This model assumes that there is a strong coupling to a singly lattice coordinate, which is taken to be representative of the displacements of neighboring ions. Usually it is assumed that these neighboring ions are in a totally symmetric "breathing" mode. In practice, the "single" frequency may turn out to be an average of many phonon mode frequencies,

or perhaps a "local" mode, one that is unrelated to the crystal lattice. At other times, one phonon frequency may so dominate all other modes that a single mode approximation is very valid.

The general concept of the SCC model is shown in Figure 4. The ground state and first excited state of an ion are displayed as harmonic oscillators, with a single dominate phonon energy for each state. The excited state can be somewhat offset from the ground state, as measured by the configuration coordinate Q. This offset is referred to as Franck-Condon offset, and is designated as q_o. A zero-phonon transition would go from the lowest level of one state directly to the lowest level of the other state and have energy E_o. The probability that such a transition occurs is directly related to the measure of q_o. If q_o is large, the probability of such a zero-phonon transition is extremely small. Where such a transition can be seen experimentally, it serves to fix the energy relationship of the two parabolas.

Assuming some Franck-Condon offset occurs, one expects to see phonon assisted transitions, which are displaced from the zero phonon line. This is due to an effect known as the adiabatic approximation, which states that a transition between ground and excited states occurs so rapidly that the lattice, even though in constant thermal vibration, appears frozen during the transition. Thus a transition is represented as a vertical line from the lowest level of the state to the other parabola. The figure shows both a phonon assisted absorption, going from the lowest level of the ground state to the excited state parabola, and also an emission, from lowest level of the excited state to the ground state parabola. These are considered

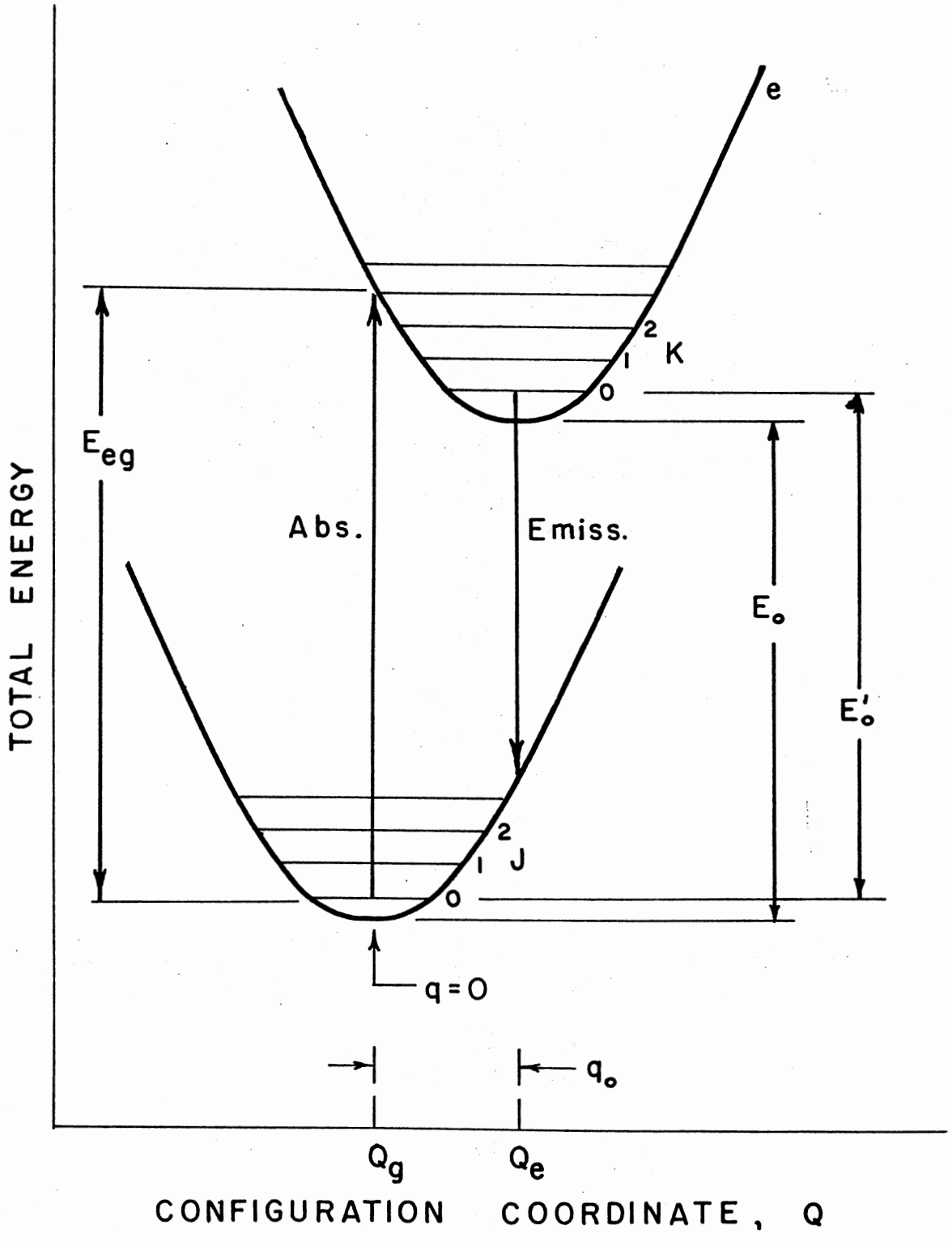

Figure 4: Generalized Configuration Coordinate Diagram

phonon-assisted, because once the transition is made, phonons are given off to reduce the energy to the lowest level of that state. As can be seen from the figure, the absorption energy, E_{eg} exceeds the zero-phonon energy E_o, while the emission energy E_o' is less than E_o. Because of the probabilities of the transitions, E_{eg} represents the energy peak of the broadband absorption, and E_o' is the peak of the broadband emission.

Not only is it possible to treat the broadening of absorption and emission bands with the SCC model, it is also the aim of several authors to picture radiative and non-radiative relaxation rates from excited states using the some model. Briefly, the simplest approach to this problem was done by Kiel (60), who considered the case in which there was no Franck-Condon offset, nad that the two parabolas were identical in shape, i.e., that the two oscillators had identical force constants. Huang and Rhys (61) relaxed the constraint of zero offset, but still assumed equal force constants. More recently, Struck and Fonger (55) have treated the general case of no constraints on either offset or force constants. We will use their analysis later for MgF_2:Ni, and thus will examine it here.

Let us begin describing the dynamic behavior of the multiphonon (or phonon assisted) process with two transition rates: the radiative rate R_R and the non-radiative rate R_{NR}. These rates determine the quantum efficiency, η, and the lifetime, τ.

$$\eta = \frac{R_R}{R_R + R_{NR}} \qquad (2)$$

$$\tau = \frac{1}{R_R + R_{NR}} \tag{3}$$

In the past, several methods have been used to determine R_R and R_{NR} experimentally. Direct measurement applies in only a few cases because it is difficult in general to measure the quantum efficiency. Flaherty and DiBartolo (62) described a direct method based upon relative efficiencies at different temperatures. Weber (64) calculated R_R, measured τ, and obtained R_{NR} from equation (3). The method we use here involves measuring the temperature dependence of the lifetime. Because R_R can be assumed to be temperature independent and R_{NR} can be described by suitable theories, a fit of the measurements using the above equations gives values for R_R and for other parameters introduced by the theory.

Analysis of Struck and Fonger

The system by Struck and Fonger (55) is based on a Quantum Mechanical SCC model, as shown in Figure 5. The quantum numbers, wave functions, and phonon energies for the u and v parabolas are n, u_n, $\hbar\omega_u$ and m, v_m, $\hbar\omega_v$, respectively. The model is taken in the thermal-Condon approximation that the initial vibrational states are in thermal equilibrium and the $v_m \rightarrow u_n$ rate is proportional to the squared overlap integral $\langle u_n | v_m \rangle^2$. This gives prescriptions for the radiative and nonradiative rates as follows:

$$R_R = R_{nm} = R_{uv} (1-r_v) r_v^m \langle u_n | v_m \rangle^2 \tag{4}$$

$$R_{NR} = N_{nm} = N_{uv} (1-r) r_v^m \langle u_n | v_m \rangle^2 \tag{5}$$

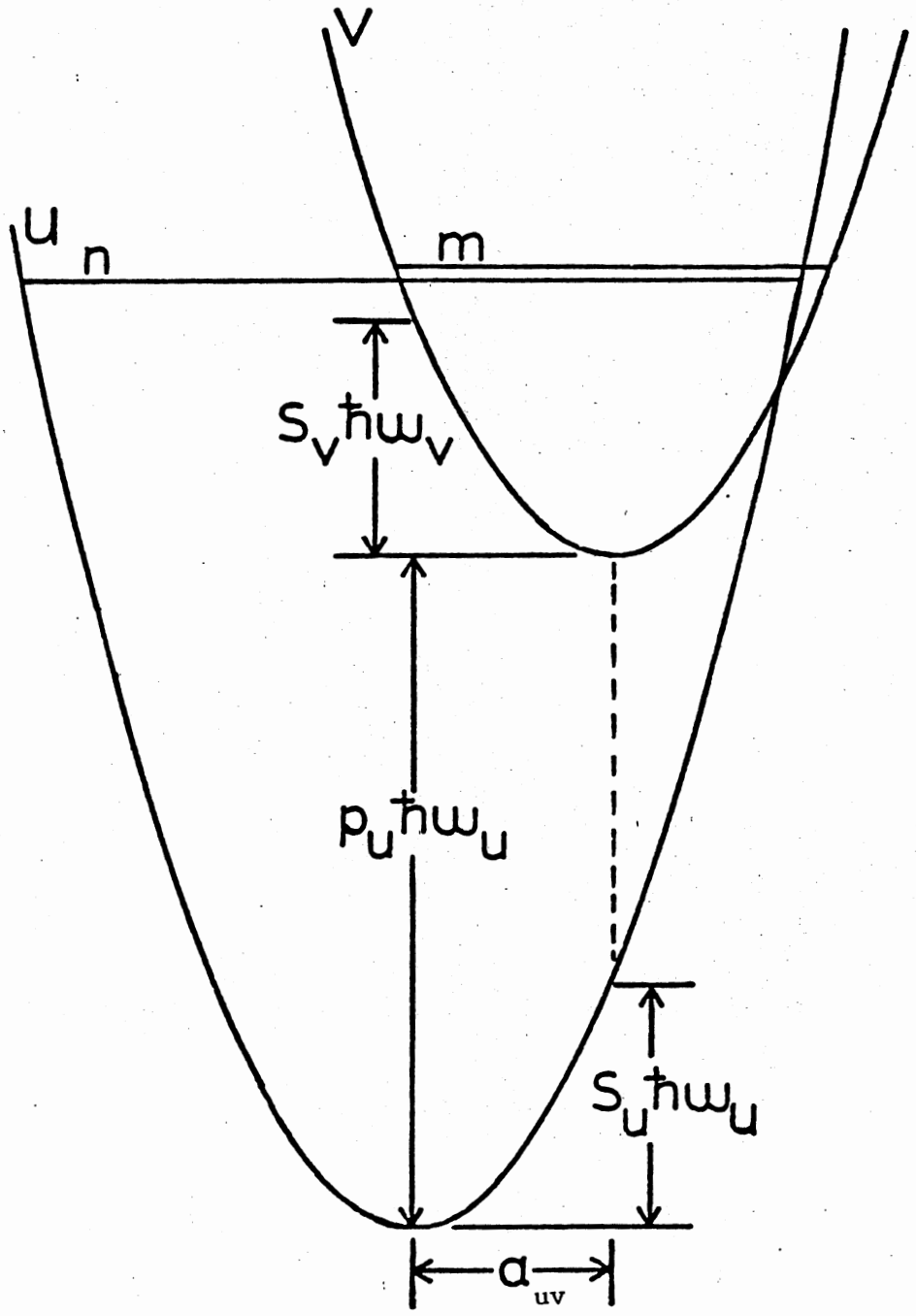

Figure 5: Struck and Fonger Radiationless Relaxation Model

where R_{uv} and N_{uv} are constants from the electronic portion of the transition integral, and $r_v = \exp(-\hbar\omega_v/kT)$ is the Boltzmann factor for levels in the excited state v. Thermal weights are then given by $(1-r_v)r_v^m$.

We now try to compute the change of R_{NR} with temperature, remembering that R_R has significantly less dependence on temperature because the constant R_{uv} is several orders of magnitude smaller than N_{uv}. The computation depends on seven parameters which are related to experimental results. These seven are: T, the temperature; $\hbar\omega$, the interaction phonon energy; p_u, the number of these phonons emitted over the energy gap of interest; a_{uv}, the Franck-Condon offset of the two parabolas in length units; θ, which is related to the ratio of the phonon energies for states v and u; and R_{uv} and N_{uv}, defined above. A copy of the computer program, written in BASIC to be run on the HP-85 computer, is included in the appendix.

For the 3-d impurity ions, the parameter θ is found to be within a few degrees of 45^o, which means that the two states have nearly equal force constants. Struck and Fonger define θ as:

$$\tan^2 \theta = \frac{\hbar\omega_v}{\hbar\omega_u} \tag{6}$$

The value chosen for h in the program is then really $\hbar\omega_v$, but the two values will be very close because θ is near 45^o.

Finally, a_{uv} is related to the displacement of the broad band peaks of the absorption and emission. We find the relationships to be:

$$S_v^{1/2} = \frac{A_{uv} \sin \theta}{\sqrt{2}} \tag{7}$$

and

$$S_u^{1/2} = \frac{A_{uv} \cos \theta}{\sqrt{2}} \tag{8}$$

so that

$$A_{uv}^2 = 2(S_u + S_v) \tag{9}$$

S_u and S_v are alternative measures of the Franck-Condon offset, and for the case of $\theta=45^o$, reduce to the common value $S_u=S_v\equiv S_o=a^2_{uv}/4$, which is also called the Huang-Rhys factor. For the 3-d ions, a first approximation of the value of a_{uv} is found by assuming $\theta=45^o$, and using the value of S_o.

Now the values of the overlap integrals may be computed by use of the Manneback recursion formulas (64), in which A_{nm} is the overlap integral $\langle u_n | v_m \rangle$. The relations depend on the parameters θ and a_{uv}, as shown below:

$$A_{oo} = \sin 1/2\ 2\theta \exp\ (-1/8 \sin^2 2\theta\ A_{uv}^2) \tag{10}$$

$$(m+1)^{\frac{1}{2}}A_{n,m+1} = -m^{\frac{1}{2}}\cos 2\theta A_{n,m-1} - \frac{1}{\sqrt{2}}a_{uv}\sin 2\theta\cos\theta\ A_{n,m} \tag{11}$$

$$+ n^{\frac{1}{2}}\sin 2\theta\ A_{n-1,m}$$

$$(n+1)^{\frac{1}{2}}A_{n+1,m} = n^{\frac{1}{2}}\cos 2\theta\ A_{n-1,m} + \frac{1}{\sqrt{2}}a_{uv}\sin 2\theta\sin\theta\ A_{n,m} \tag{12}$$

$$+ m^{\frac{1}{2}}\sin 2\theta\ A_{n,m-1}$$

Thus for given θ and a_{uv}, the rates given by equations (4) and (5) may be computed, but they tend to be unwieldy because they are double indexed. Struck and Fonger then apply an averaging technique to obtain the simple, one-dimensional optical-band shapes that are seen in experiments. This averaging would not be acceptable if one were studying, say, fine structur, but are useful in our examination of the thermal quenching of emission. This method of averaging is based on reductions of phonon energies to those equally spaced energies which occur naturally for $\theta=45^{o}$ and T=OK.

From the SCC model in Figure 5, it can be seen that the radiative and non-radiative energy balances are:

$$h\upsilon_{zp,vu} + m\hbar\omega_{v} - n\hbar\omega_{u} + h\upsilon_{nm} = 0 \qquad (13)$$

$$h\upsilon_{zp,vu} + m\hbar\omega_{v} - n\hbar\omega_{u} = 0 \quad \text{for } v_{m}\rightarrow u_{n} \qquad (14)$$

In the case of $\theta=45^{o}$, $\hbar\omega_{u}=\hbar\omega_{v}=\hbar\omega_{o}$, and all radiative transitions with the same quantum number $p_{u}\equiv n-m$ will fall at the same photon energy $\hbar\omega_{pu}$ so that:

$$h\upsilon_{zp,vu} - p_{u}\hbar\omega_{o} + h\upsilon_{pu} = 0 \qquad (15)$$

and all non-radiative transitions have the particular quantum number p_{u} defined through equation (14) as:

$$h\upsilon_{zp,vu} - p_{u}\hbar\omega_{o} = 0 \qquad (16)$$

Thus, all transitions with this same quantum number p_u may be grouped into a single unit with the summed thermal-Franck-Condon weight:

$$W_{pu} = \sum_{m=m_o}^{\infty} (1-r_v)\, r_v^m \langle u_{pu} + m | v_m \rangle^2 \qquad (17)$$

for $p_u = 0,\pm1,\pm2,\ldots$, and m_o is the larger of 0 and $-p_u$. Radiative and non-radiative transitions are then described by the one-dimensional distribution W_{pu} which is indexed by p_u.

For the general case $\theta \neq 45^o$ and $T \neq 0K$, we may use this same approach by introducing a new integer quantum number $p_U = 0,\pm1,\pm2,\ldots$ That approximates $n-(\hbar\omega_v/\hbar\omega_u)m$ and also new effective Franck-Condon weight factors U^2_{pUm} defined by:

$$U^2_{pUm} = f_m \langle u_{pU} + i_m - 1 | v_m \rangle^2 + (1-f_m) \langle u_{pU} + i_m | v_m \rangle^2 \qquad (18)$$

where i_m is the smallest integer greater than or equal to $(\hbar\omega_v/\hbar\omega_u)m$, and the fraction f_m is such that

$$i_m = (\hbar\omega_v/\hbar\omega_u)m = f_m \qquad (19)$$

For p_U negative, U^2_{pUm} is zero unless $p_U + i_m \geq 0$. For this approximation, all transitions with the same quantum number p_u are unresolved transitions at nearly the same energy and can be treated as a single unit. The summed thermal-Franck-Condon weight for this unit is:

$$u_{pU} = \sum_{m=m_o}^{\infty} (1-r_v)\, r_v^m\, u^2_{pUm} \qquad (20)$$

where $m_o=0$ for $p_U \geq 0$ and p_U negative, is the smallest index for which $p_U + i_m = 0$.

Then, the transition rates given by equations (4) and (5) can be computed as:

$$R_R = R_{uv}\, u_{pu} \text{ and } R_{NR} = N_{uv}\, u_{pu} \tag{21}$$

The energy balances are defined in a manner similar to equation (15) and (16), using our new approximate quantum number p_U.

Finally, comparison with experimental measurements of the lifetime may be made with the expression:

$$\frac{1}{\tau} = \frac{1}{\tau_o} + N_{uv}\, u_{pu} \tag{22}$$

where $R_{uv}=1/\tau_o$ is the low temperature radiative lifetime.

In all of this discussion so far, the underlying assumption has been that the SCC model itself is unaffected by temperature. For many systems, this is perhaps a reasonable assumption. However, we observe experimentally that as temperature rises, the absorption and emission bands tend to shift toward lower energy. McClure (65) explains the shift as due to thermal expansion of the lattice. The thermal expansion of the lattice changes the strength of the crystal field, causing a shift in energy levels for the defect. Sturge (66) compensates for this change by introducing anharmonicity in the oscillators of the 10^{22} lattice modes. The basic result is that as temperature of the lattice increases, the v-parabola tends to descend relative to the u-parabola.

In trying to fit the lifetime data, it becomes difficult to account for this gradual change of energy levels. As a first approximation to this shift, in our computer program, we introduced a temperature at which the v-parabola had moved down by an energy $\hbar\omega$, then adjusted the parameter p_U to be one less than it was at lower temperatures. While this is only a rough approximation to the actual gradual shift, there is a noticable improvement in the fit to the data, as will be reported in later discussion.

Energy Transfer Process

The discussion thus far has assumed that absorption and emission take place at single lattice sites. Experimentally, we notice, however, numerous cases where two or more ions are involved in the absorption and emission of photons. The term energy transfer is normally applied when one type of ion, called the sensitizer (S), transfers energy that it has to a second type of ion, known as the activator (A). If the energy level of the sensitizer and activator overlap, then the process is referred to as resonant energy transfer. Other situations can arise where the energy level of the sensitizer is higher than for the activator, and phonon-assisted energy transfer results. It is possible, but less probable, that energy transfer can take place when the sensitizer level is below the activator level. We will not examine that case here. Discussions of energy transfer processes are found in review articles by Watts (67), Reisfeld (68), Wright (69), and Riseberg and Weber (70).

In Figure 6 we see the two energy transfer cases shown schematically. On the left side of the figure is resonant energy transfer,

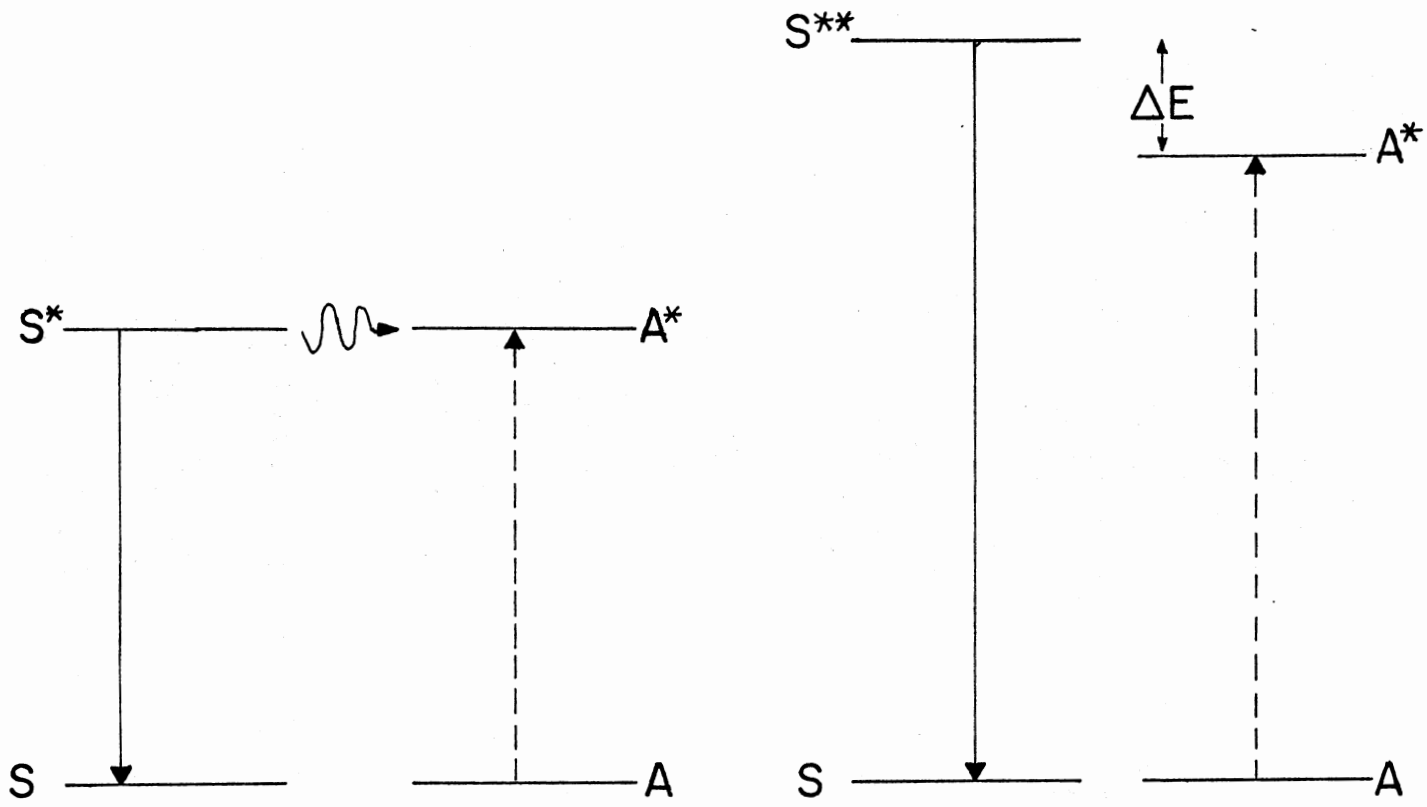

Figure 6: Resonant and Phonon-Assisted Energy Transfer

where the sensitizer emission band overlaps with the activator absorption band. In this case there is also the possibility that the emission of the sensitizer may be radiatively reabsorbed. However, this may be easily detected experimentally, and is found to be of consideraly less importance than the non-radiative transfer of energy from S→A. Forster (71) and Dexter (72) have worked out the rate of non-radiative transfer as:

$$P_{SA} = \frac{2\pi}{\hbar} \left| \langle S^*A | H_{int} | SA^* \rangle \right|^2 \int g_S(w)\, g_A(w)\, dw \qquad (23)$$

where the quantum numbers for the states are S and A. The terms $g_S(w)$ and $g_A(w)$ are the two spectral line shape functions of the transitions S*→S and A→A*. This formula is valid only for resonant energy transfer because the integral involving the overlap of the sensitizer and activator energy bands goes to zero as the difference between the energy level increases.

The interaction Hamiltonian is usually written in terms of an electric multipole or exchange interaction. The resultant range dependence of the energy transfer probability P_{SA} is:

$$P_{SA} = \frac{1}{\tau^o_s} \left(\frac{R_o}{R} \right)^n \qquad (24)$$

where n=6 for dipole-dipole interactions, n=8 for dipole-quadrapole interactions, and n=10 for quadrapole-quadrapole interactions. The lifetime of the sensitizer without the activator is τ^o_S, while R_o is the critical transfer distance which is proportional to the

overlap integral of equation (23) to the (1/n) power.

Phonon assisted energy transfer may occur when there is an energy difference (ΔE) between levels S** and A*, as shown in the right hand portion of Figure 6. The theory for this was first developed by Orbach (73) and worked out in detail by Miyakawa and Dexter (74), and Orbach (75). For this phonon assisted energy transfer, the probability P_{SA} is given by Orbach as:

$$P_{SA} = \frac{2\pi}{h} \left| \langle S^*A \left| H_{int} \right| SA^{**} \rangle \right|^2 K \begin{Bmatrix} n \\ n+1 \end{Bmatrix} \int g_S(w)\, g_A(w \pm \hbar\omega) dw \qquad (25)$$

where K is a combination of electron-phonon matrix elements, n is the phonon occupation number, and the plus and minus signs refer respectively to the phonon absorption or emission in the energy transfer process.

For the case of nickel ions in an MnF_2 host, one expects to find some energy transfer between the levels of Mn^{2+} and the $^3T_{1g}$ and $^1T_{2g}$ levels of the Ni^{2+}. In particular, since the overlap of the $^4T_{1g}$ level of Mn^{2+} and the $^1T_{2g}$ level of Ni^{2+} is so strong, there is a strong likelihood of resonant energy transfer between these levels. That gives the prospect of an enhanced emission of the Ni^{2+} ion, and also the possibility of improved efficiency by using the manganese host. We will look at these possibilities in detail in chapter 5.

CHAPTER III

EXPERIMENTAL EQUIPMENT AND PROCEDURE

The crystals used in this study came from several sources. Pure MnF_2 was obtained commercially from Harshaw Chemical Company. MgF_2 doped with nickel was furnished by the courtesy of Fahey of Lincoln Laboratory, MIT; other boules of the same crystal were purchased from Optovac, Incorporated, as were crystals of MgF_2:Co. Mr. Walter Hargreaves of Optovac, Inc., donated two single crystal pieces of nickel-doped MnF_2, and two boules of cobalt-doped MnF_2 were grown in the OSU Ctystal Growth Facility.

Crystals were oriented by Z. Al-Shaieb with an optical polarizating microscope and cut with the c-axis either parallel to the surface ($C_{\parallel}$) or perpendicular to the curface ($C_{\perp}$) using a diamond saw. Surfaces were polished by hand lapping on successively finer polishing paper obtained from Buehler, Ltd. The final polishing was done with 3 micron grit in water.

For low temperature measurements, the samples were mounted in either a Cryogenic Technology, Inc., Model 20 cryogenerator capable of reaching 15 K, or a Sulfrian liquid helium cryostat. Temperature was measured to ±2 K by means of a gold-iron versus chromel thermocouple. Sample temperatures in the cryogenerator could be varied continuously from 15 K to room temperature by means of a 15 Watt

heater, and a temperature controller allowed the maintenance of any desired temperature for any desired period of time. A schematic of the temperature controller is shown in Figure 7.

Optical absorption measurements were made with a Cary 14 spectrophotometer, which records optical density as a function of wavelength over a range of 200 nanometers to 2.5 micrometers. The optical density is the base 10 logarithm of the ratio of the incident to transmitted light. The Cary 14 uses a double-beam system to provide both intensities simultaneously as a function of wavelength. The absorption coefficient is related to the O.D. by:

$$\alpha = \frac{(2.303)\ \text{O.D.}}{t} \tag{26}$$

where t is a sample thickness in cm. Normally α is plotted against photon energy or wavelength.

Polarized absorption measurements are also possible on the Cary 14. For visible and ultraviolet measurements, to a limit of about 250 nm, Polaroid type HNP'B unsupported polarizers were inserted in front of the beam splitter. Thus both the sample beam and the reference beam used the same polarizer. For infrared measurements, Polaroid type HD infrared polarizers were used in a similar manner.

Luminescence, excitation, and lifetime measurements were made using the equipment indicated in Figure 8. Excitation was by a 75 Watt short-arc Xenon lamp from Illumination Industries. The light was focused by quartz lenses onto the slits of a 22 cm Minimate monochromator from Spex Industries. Two gratings can be used in the Minimate. One grating has 1200 grooves with a dispersion of 40 A/mm,

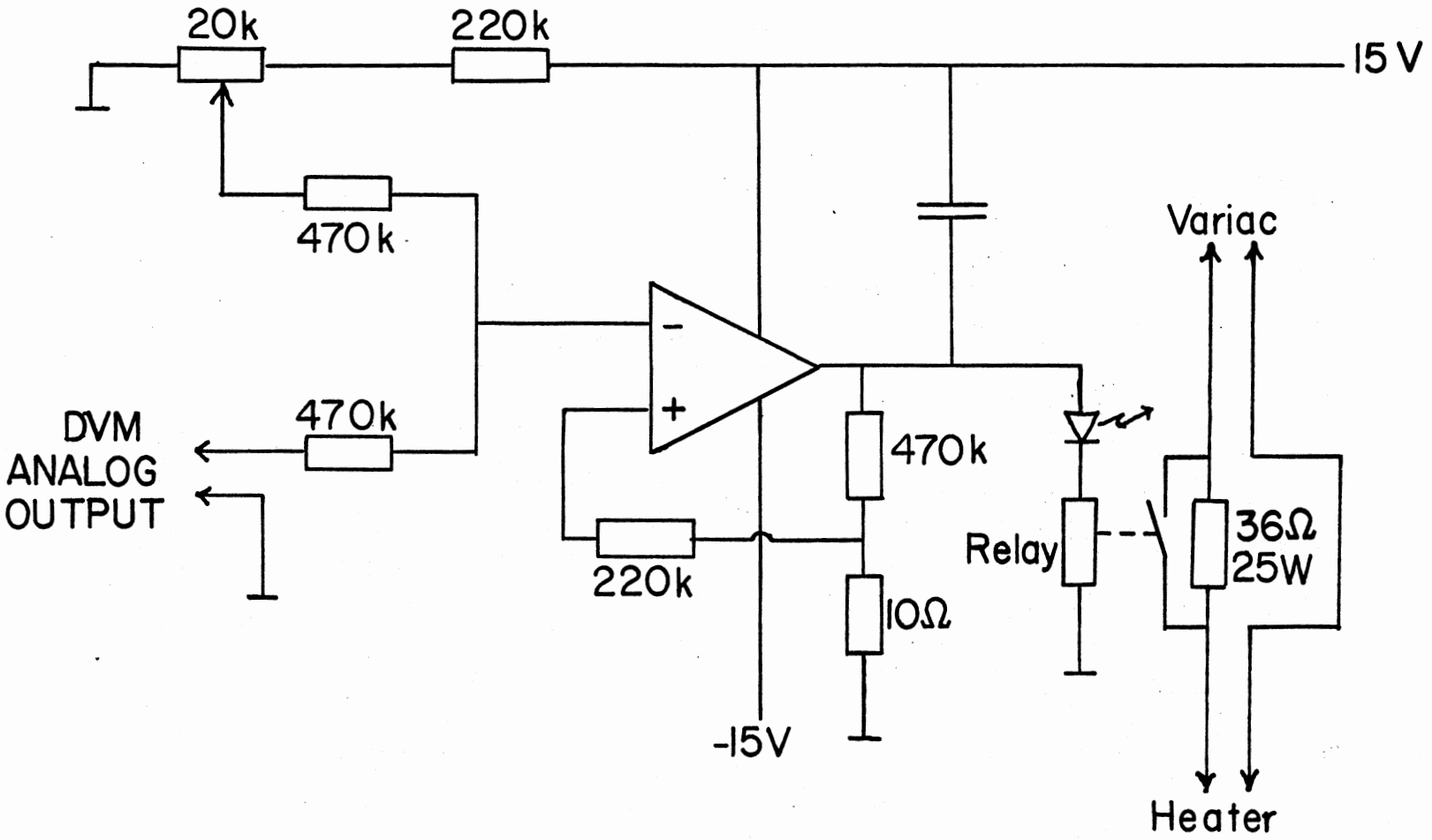

Figure 7: Schematic of Temperature Controller

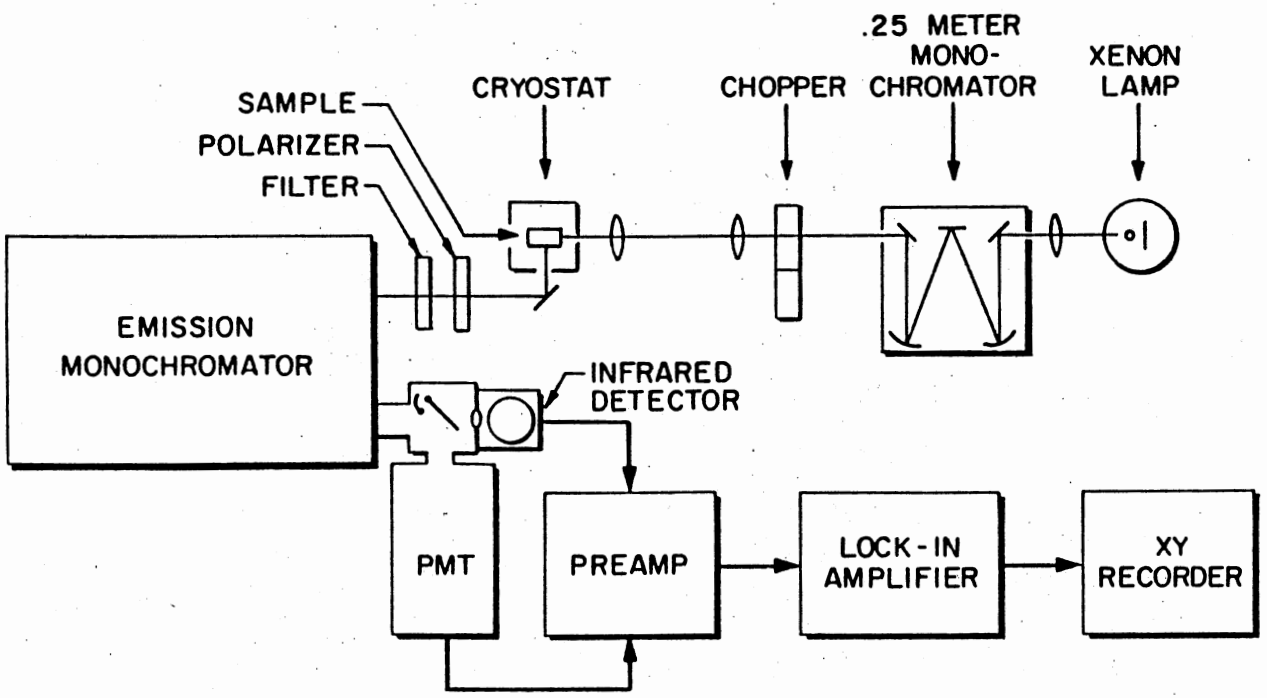

Figure 8: Block Diagram of Visible and Infrared Luminescence Apparatus

and is blazed at 300 nm; the other is a 600 groove grating blazed at 750 nm with a dispersion of 80 A/mm. The 1200 groove grating has a usuable range from about 200 nm to about 800 nm. The 600 line grating is usable from about 400 nm to about 1.5 μm.

The light is focussed onto the sample by quartz lenses, and when thick samples are used (2 mm or more) the sample is mounted so that the exciting light is incident on the edge and the emission is gathered from the front surface. For thin samples, the sample is turned to about 40^{o} to the incident light, and the emission is taken from the same surface. In both cases, care is excercised to reduce scattered light entering the emission monochromator. Calcium fluoride lenses are used to focus the flourescence onto the slits of the emission monochromator, which is a .75 m Spex Model 1702, have a 600 groove grating blazed at 1.6 μm. with a dispersion of 20 A/mm.

The light is detected by either a cooled PbS detector (Optoelectronics OTC-22-53TXX) or a cooled phototube (an RCA C-31034, an RCA-7102, or an EMI-9659). The 7102 tube is used for measurements near 1μm and is normally cooled with dry ice. The other two tubes are used for visible and ultraviolet emissions, and are cooled to about $-30^{o}C$ with a Pacific Photometric Model 33 thermoelectric cooler. The cooling allows the increased sensitivity of high voltage operation by reducing the noise (dark current).

The output of the phototube is amplified by a Keithly Model 427 Current Amplifier, and processed by a Keithly Model 840 lock-in amplifier. The reference signal is provided by chopping the light in either the exciting beam or immediately after the sample. The choppers are variable in frequency, and can be controlled from about

5 Hz to 700 Hz. When using the PbS detector, the preamp is a Keithly Model 103A Nanovolt Amplifier, but the same lock-in amplifier is used. High voltage for the phototube is provided by a Fluke Model 412A High Voltage Power Supply, and for the PbS detector by a Fluke Model 301E Precision DC Power Supply producing 145 volts and smoothed by a filtering circuit.

The output of the lock-in amplifier is normally displayed directly onto a Houston Instruments recorder (Model 2000) although for very weak signals it is possible to average over many scans by storing the information in a Nicholet Model 1070 Signal Averager. The signal-to-noise ratio of the fluorescent signal goes as the square root of the number of scans, so averaging is at times extremely useful, although somewhat tedious. The stored signal from the Nicholet is likewise displayed on the X-Y Recorder.

The Nicholet has an additional use when measuring lifetimes. The Nicholet samples at set time intervals; those intervals are chosen by the user. Thus we can measure the signal as a function of time from some triggering point, and store that information repeatedly to build up a picture averaged over many scans. This picture is displayed on a Tektronix display oscilloscope, and hard copy may be output to the x-y recorder. The exponential decay curve of the lifetime display is rendered into a "straight" line by a Type 14 logarithmic module plugged into the Y-axis of the Houston Instruments recorder. This data is linearly fit and the lifetime measured as the 1/e value of the line. Limitations on the ability of the system to measure lifetime depend on the detector; the PbS has an intrinsic response time of 1.5 μsec when cooled, and so shorter

lifetimes than this for infrared signals cannot be measured. For visible signals, the phototube is so fast the risetime of the pre-amplifiers becomes the limiter; the Keithly preamp is limited to about 10 μsec as its risetime. Other, faster amplifiers have significantly lower gain and are not always usable. The Nicholet is limited by its own electronics to dwell times on the order of 10 μsec, but this can be overcome by using a Biomation Model 610B Transient Recorder to store single scans and then digitally transfer the data to the Nicholet for averaging. The Biomation is capable of 100 nanosecond dwell times. This puts an effective limit on our lifetime measurements of about 1 μsec under optimum conditions.

For high resolution work in the visible and ultraviolet portion of the spectrum, a second rig is available which has been described at length previously (76,77). A block diagram is shown in Figure 9. It features a 1-meter Jarrell-Ash monochromator with an 1180 groove/mm grating and dispersion of 8.2 A/mm. An RCA-C31034 phototube is used, and the exciting source is a 300 Watt Xenon lamp made by Illumination Industries. The electronics are a Keithly Model 427 Current Amplifier, followed by a Keithly Model 840 Auto-Loc Amplifier. The reference signal comes from a Keithly Model 8403 light chopper, which chops the exciting light at 90 Hz. Quartz lenses are used throughout the system, and the Minimate has a 1200 groove grating identical to the one described earlier in this section.

Where necessary, sharp cut-off filters (long-wave-pass) bought from Hoya Optics were used in the emission beam to cut off the exciting light. Additionally, for IR-emission, a piece of high-purity germanium, polished to enhance the IR-transmissions, was used

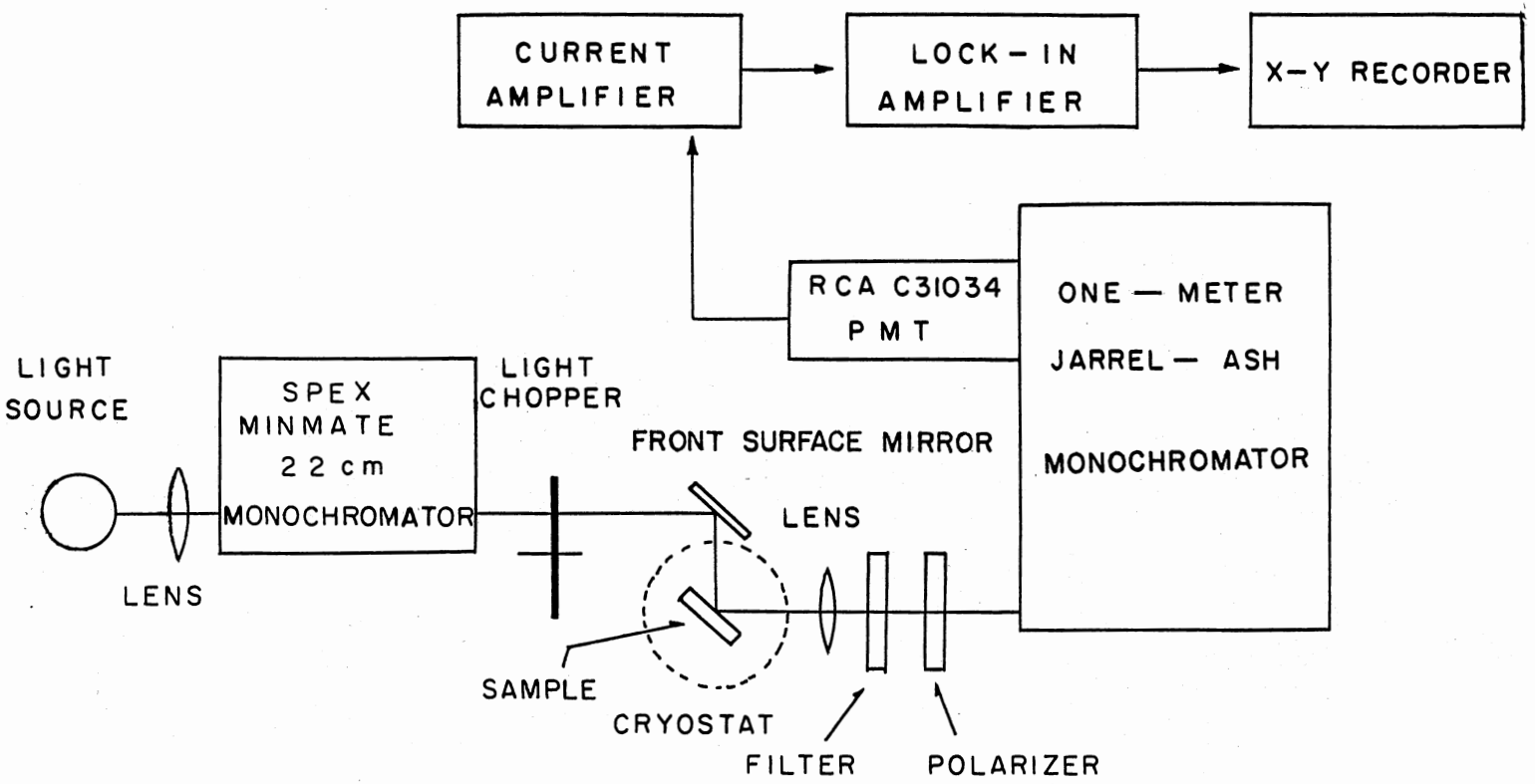

Figure 9: Block Diagram of High Resolution Luminescence Appartus

for signals of wavelengths greater than about 1.2 μm.

Calibration of the optical system was accomplished by using a Spectra Model 310 Radiometer (in the range from 430 nm to 930 nm) and also a GE QL-157 quartz-iodine standard lamp. Both have calibration traceable to the National Bureau of Standards. Both excitation and emission spectra were corrected, where appropriate.

CHAPTER IV

RADIATION DAMAGE IN PURE MgF_2

The $F_2(C_{2h})$ Center

The center which appears to be the most well identified in MgF_2 aside from the F center is the $F_2(C_{2h})$ center (22,26). This center has been designated as being responsible for the optical absorption that occurs around 260 nm and 375 nm and the emission at 420 nm. The absorption and emission bands from this defect are highly polarized with $E \perp C$. Figure 2 illustrates schematically the MgF_2 lattice and the four possible F_2-center configurations which are shown by solid lines. For the $F_2(C_{2h})$ center polarized absorption and emission is expected. Figure 10 portrays the excitation and emission spectra from this particular defect in MgF_2. Note that when the electric vector of the incident light is parallel to the C-axis, $E \parallel C$, as shown by the dashed lines, there does appear to be some absorption in both the 260 nm and 370 nm regions. It will be shown later that this apparent absorption in the 370 nm region comes from another type of defect which also has a small unpolarized emission underneath the 420 emission of the $F_2(C_{2h})$ center. The temperature dependence of both the absorption half-width and the emission half-width has been studied previously (24). An analysis of the temperature dependence reveals that the dominant phonon made interacting with the ground state of

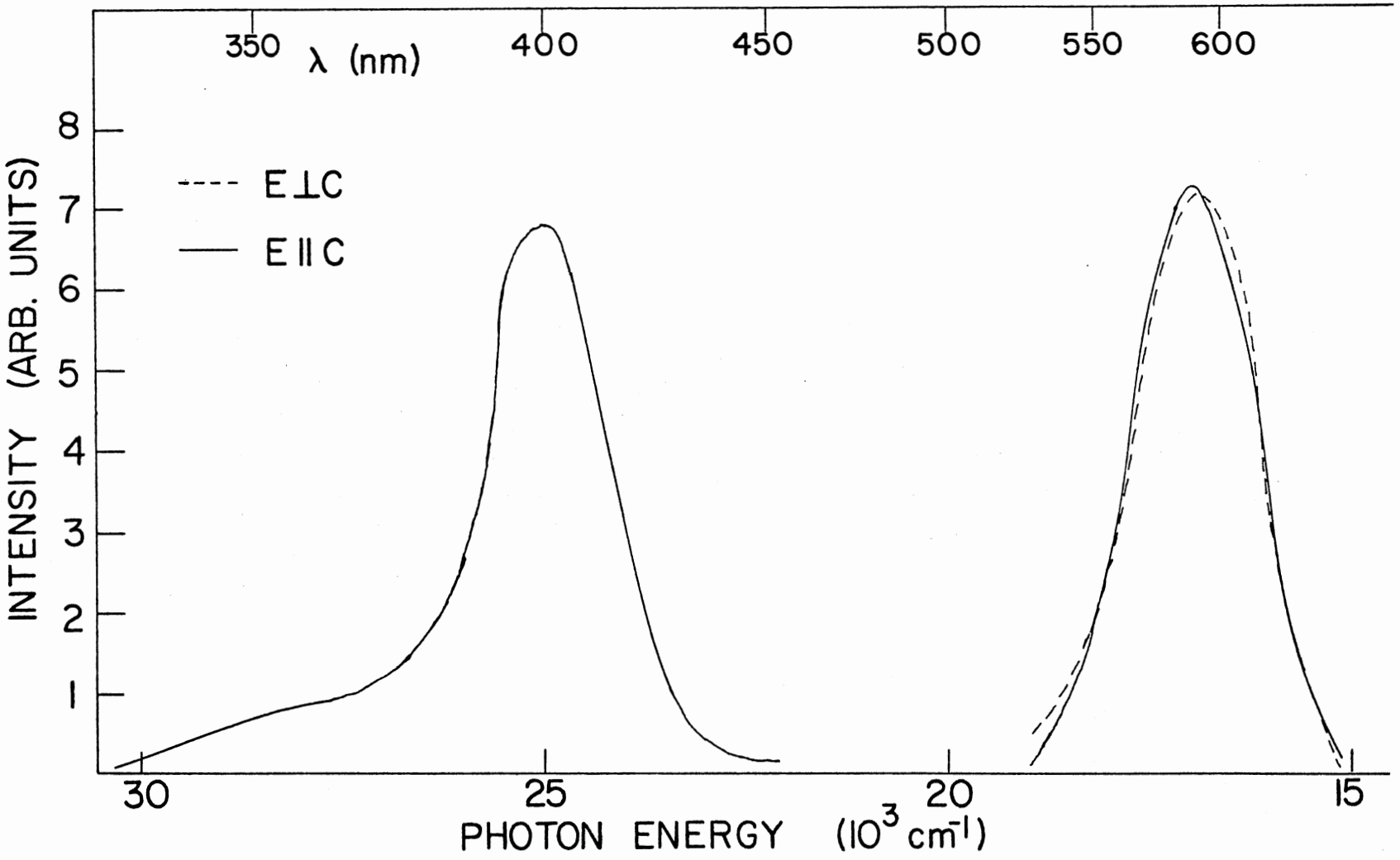

Figure 13: Excitation and Polarized Emission Spectra for the 600 nm Band in MgF_2

this defect has an energy of 280 cm^{-1} whereas in the excited state the dominant phonon mode is 175 cm^{-1}. This analysis is based on the work of Keil (78), whose work on transition probabilities allows the development of an expression for the full width at half maximum as a function of temperature for absorption bands. This expression is:

$$H(T) = H(0) \left[\text{csch } \left(\frac{\hbar\omega}{2kT}\right)\right]^{\frac{1}{2}} \tag{27}$$

where H(T) is the half width (i.e., full width at half maximum) at temperatur T, and H(0) is the half width at zero, and $\hbar\omega$ is the phonon energy. The half width at 0^{o} K is predicted to be:

$$H(0) = 2.36\ S^{\frac{1}{2}}\ \hbar\omega \tag{28}$$

with S being the Huang-Rhys factor. As a comparison, the expression for half width as a finction of temperature is found semi-classically (16) to be:

$$H(T) = H(0) \left[\coth \left(\frac{\hbar\omega}{2kT}\right)\right]^{\frac{1}{2}} \tag{29}$$

which is indistinguishable from (27) in practice. Analysis then is made by plotting arc coth $\left[H^2(T)/H^2(0)\right]$ vs. 1/T, which should yield a straight line through the origin fro a proper choice of H(0). The slope of this line, $\hbar\omega/2k$, is then used to determine ω, which is the average frequency of the lattice modes involved in the interaction.

$F_2(D_{2h})$ Center

From Figure 2 it can be seen that the absorption and emission from $F_2(D_{2h})$ centers should also be polarized with the electric vector of the exciting or emitted light perpendicular to the C-axis. Figure 11 is a composite drawing of data taken by exciting an MgF_2 crystal containing large concentrations of aggregate centers at different wavelengths and measuring both the excitation spectra and the emission spectra by this technique. In some instances it was necessary to do several excitation spectra for different wavelengths and in other cases it was necessary to stimulate emission from several different excitations in order to obtain this composite diagram. This was necessary because the $F_2(C_{2h})$ center described in the section above has such a large absorption and emission intensity compared to the other centers in these crystals. In any case the dashed line illustrates data taken with $E \perp C$ in excitation and emission and it is clear that at around 320 nm a polarized excitation peak is present. Excitation into this peak gives rise to an emission at 450 nm which is also polarized with $E \perp C$. The absorption at 320 nm is extremely weak and although there have been previous hints that a small band was present at this energy, certainly without the excitation spectra technique it would not be possible to illustrate its existence. This defect, which develops with long duration optical bleaching, is a reasonable condidate for the $F_2(D_{2h})$ center. There is some apparent absorption by this defect in the 250 nm region of the spectrum but the intensity of this band is so weak it could not be investigated properly.

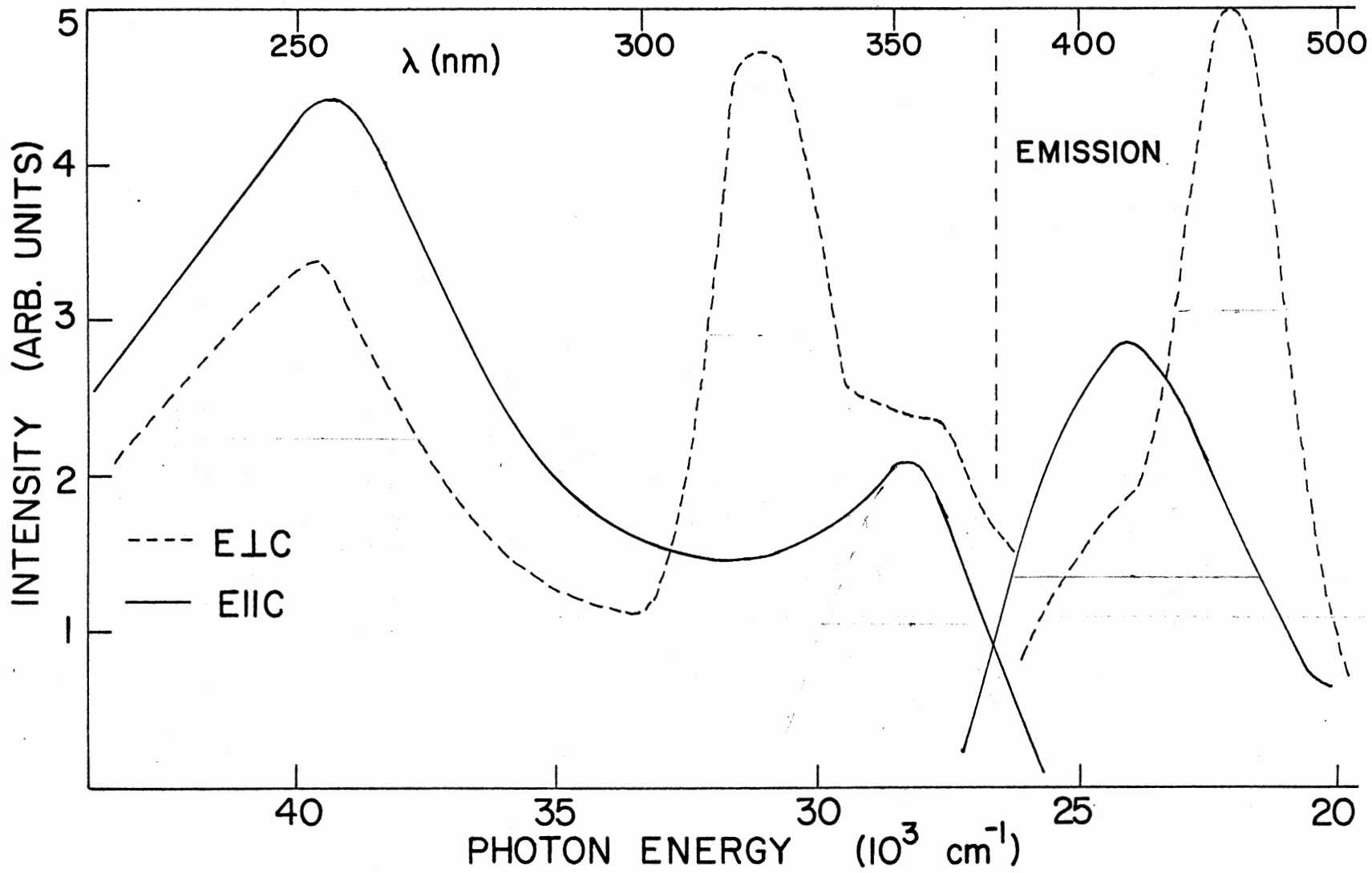

Figure 11: Polarized Excitation and Emission Spectra for 410 nm and 460 nm Bands in MgF_2

The temperature dependence of the 450 nm emission is shown in Figure 12. A dominant phonon interaction frequency of 255 cm^{-1} for the excited state can be obtained from these data.

$F_2(C_1)$ Center

It should also be noticed in Figure 11 that the solid line illustrating data for the electric vector of the instant light parallel to the C-axis and the dashed lines tend to agree in certain areas. This suggests that there is an unpolarized absorption band at around 360 nm which gives rise to an unpolarized emission at about 410 nm. There is evidence at higher energies of some absorption which also gives rise to this same emission band. Since there are 16 different orientations of the $F_2(C_1)$ type centers possible in this crystal, it would be expected that absorption and emission from this type of center would be unpolarized. The unpolarized nature of both the absorption and the emission of light from these defects suggests that this defect is the $F_2(C_1)$ center.

Other Centers

In the past a band which absorbs at 400 nm and emits light at around 600 nm has been suggested to be the $F_2(C_1)$ center. This absorption and emission is unpolarized just as would be expected for the $F_2(C_1)$ centers. However, one of the puzzling features of the band is that it is produced rapidly under the initial radiation then saturates. Optical bleaching does not enhance the band any further, whereas for most F-aggregate centers, further enhancement occurs under optical bleaching with F light. Figure 13 portrays

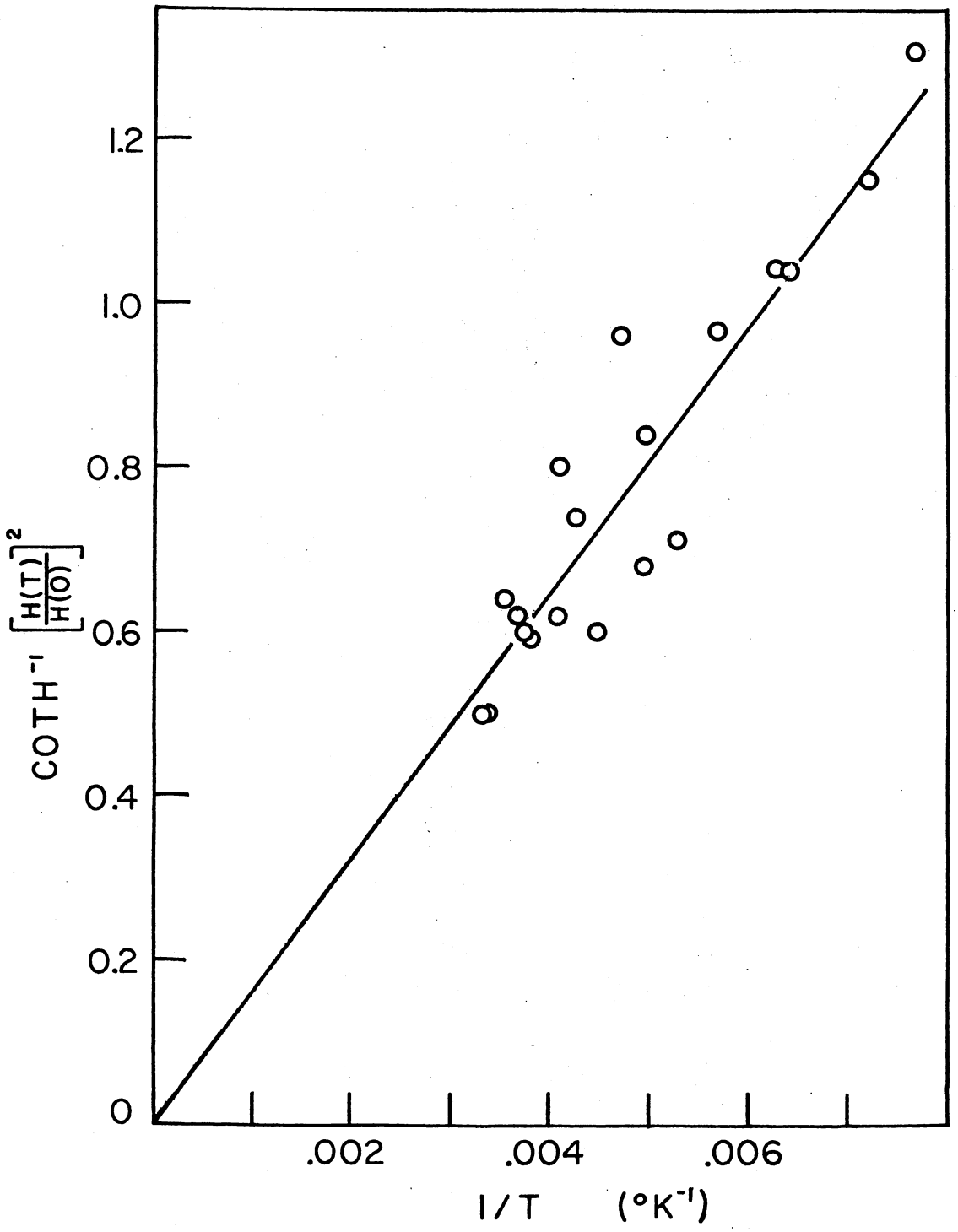

Figure 12. Arc Coth $[H(T)/H(0)]^2$ Vs. 1/T for 460 nm Emission Band

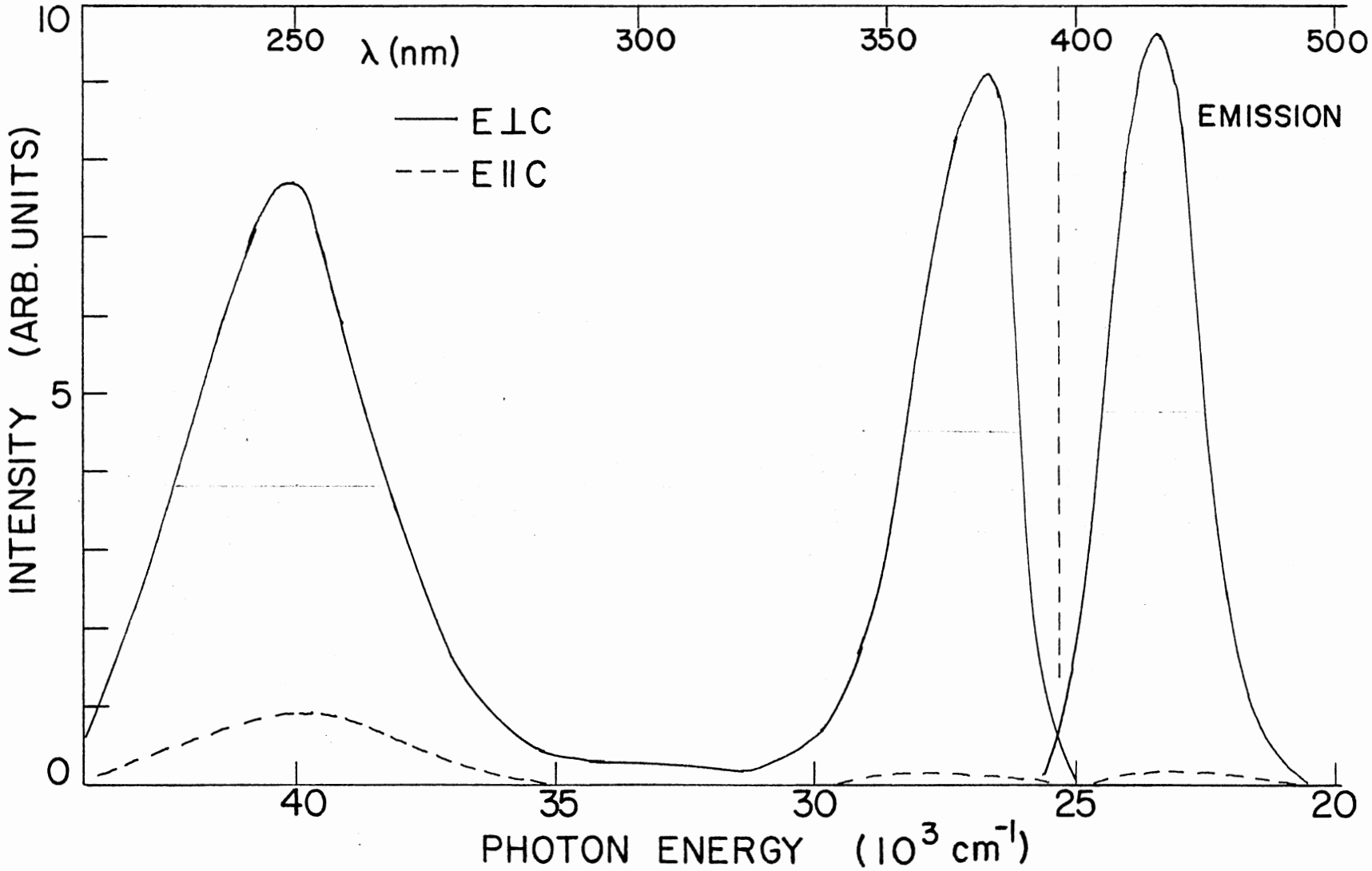

Figure 10: Polarized Excitation and Emission Spectra for 420 nm Band in MgF_2

the excitation and emission spectra for this defect. Since the absorption band saturates under radiation and bleaching it is informative to try and determine how many centers contribute to this absorption. The concentration of centers related to the absorption coefficient at the peak of the band is given by Smakula's Equations which for a Gaussian band shape is (18):

$$f N_F = 0.87 \times 10^{17} \frac{\eta}{(\eta^2+2)} W\alpha_m \qquad (30)$$

where W is the half-width of the band η=1.4 is the refractive index and α_m is the peak absorption coefficient for the band. Since the half-width of the band at 400 nm is .22 eV, and the maximum absorption coefficient is at most 20 cm^{-1} is these samples a concentration of 10^{17} centers per cm^3 would be the maximum concentration unless f, the oscillator strength, was appreciably less than one.

Another center the concentration of which does increase under optical bleaching with 254 nm light at room temperature has it peak at 300 nm and is strongly polarized E$\perp$C. This peak was also seen by Blunt and Cohen (22), who did not attempt to identify the type of defect which was responsible for it. This peak was investigated, and is found to grow in as the 360 nm band begins to saturate. However, no emission is detected from this band. Therefore, at this time, it is our suggestion that this peak could be due to F_3-type centers (three F-centers aggregating to form a cluster defect). At first it seems puzzling that an F_3-center in MgF_2 could absorb light strongly polarized with E$\perp$C axis. However, as the schematic of the MgF_2 lattice in Figure 2 illustrates, one absorption dipole

of the F_3-center would be aligned perpendicular to the C-axis if this cneter connected the two top fluorine site vacancies with one of the vacancies in the next layer. Therefore, we would expect the F_3-center to have an absorption which was strongly polarized $E \perp C$. The temperature dependence of the half-width of the absorption and emission has also been investigated as shown in Figure 14. An analysis of these data indicate that the dominant phono mode interacting with this defect has an energy of 255 cm^{-1}.

A reasonable model for analysis of F-aggregate centers in highly ionic materials is the hydrogen molecular ion approach used by Aegerner and Luty (30) to explain the F_2+-center in KCl. The basic approach is to view the F-aggregate center (F_2-center, F_3-center, etc.) as a hydrogen molecule immersed in a dielectric medium (31). The dielectric medium is characterized by a dielectric constant ε_o. The energy $E(\gamma_{AB},\varepsilon_o)$ of a given electronic state of the hydrogen molecular ion immersed in a dielectric medium (γ_{AB} is the distance between the positive charges) may be connected to the energy $E'(R)$ of the same electronic state of the molecule in free space by noting that:

$$E(\gamma_{AB},\varepsilon_o) = \frac{1}{\varepsilon_o^2} E'(R) \qquad (31)$$

with $R = \gamma_{AB}/\varepsilon_o$. An extensive tabulation of the energy levels of the hydrogen molecular ion in free space for ten electronic states over a wide range of internuclear distance R has been given by Bates, Ledsham, and Stewart (35). Therefore, for given values of γ_{AB} and ε_o, one may obtain the energy of a transition between the

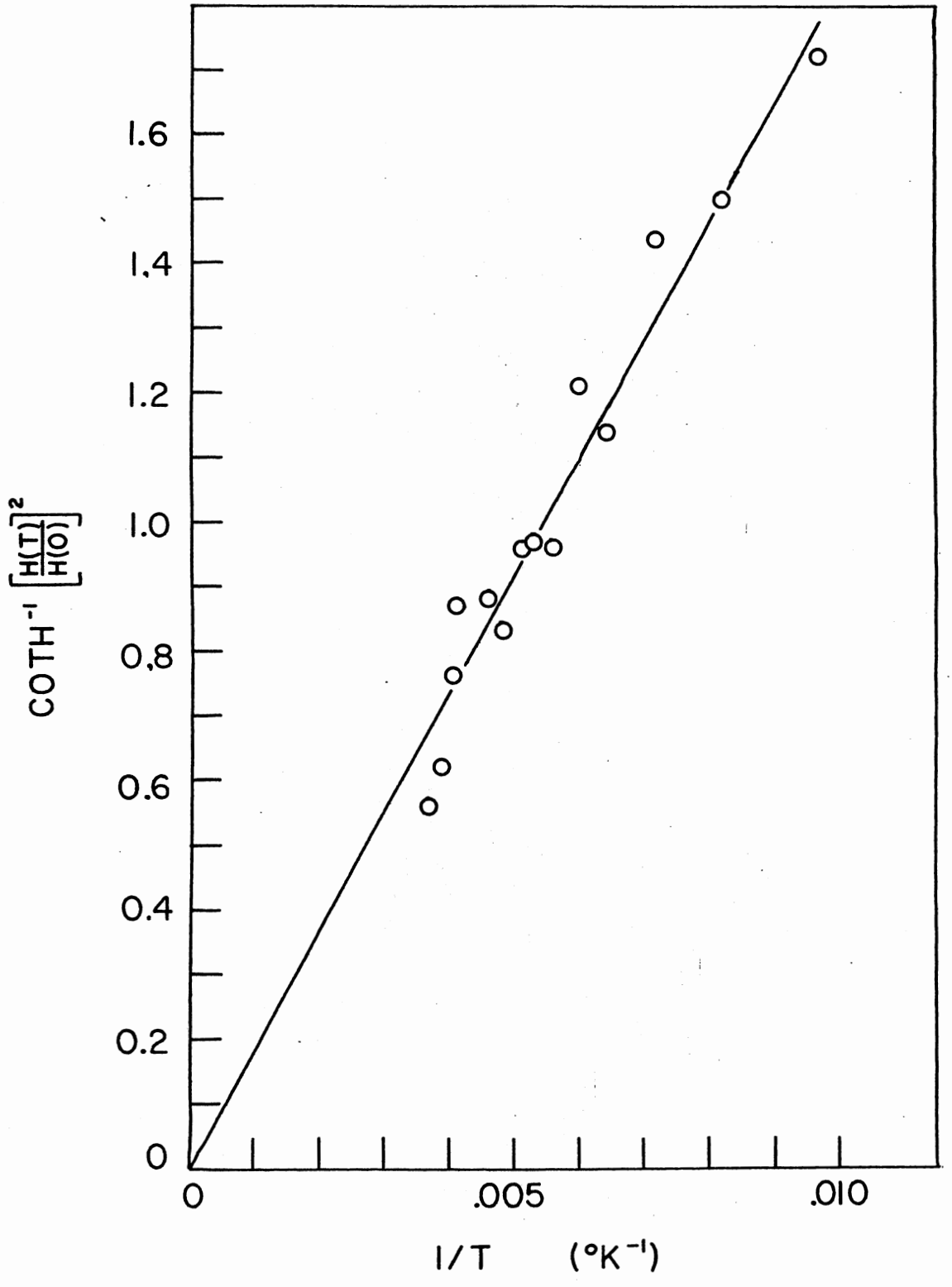

Figure 14. Arc Coth $[H(T)/H(0)]^2$ Vs. 1/T for 300 nm Absorption Band

ground state and excited states, to use for comparison with experimental values.

Table I is a compilation of this approach for several F-aggregate centers in several crystals. The crystals LiF, NaF, and $KMgF_3$ are included in the table so that one may see the validity of the model before it is applied to the F-aggregate centers in MgF_2.

In MgF_2, there are three types of F_2-centers tentatively identified in this study. The $F_2(C_{2h})$ center is felt to be the most strongly identified, and thus it was chosen to "calibrate" the model. For MgF_2, a search for the value of ε_o that would give agreement between the predicted and experimental values of peak wavelength for the $F_2(C_{2h})$ center. One expects that ε_o should be approximately equal to the square of the index of refraction (n=1.39 for MgF_2), and the value of ε_o which gave the best agreement (ε_o=1.83) was indeed close to the expected value of 1.9. The inter-ionic distance for each of the defect types was then used to determine the transition energies, with the result shown in Table I. As can be seen, good agreement with this model is obtained for identification of the 355 nm absorption with the $F_2(C_1)$ center, while the $F_2(D_{2h})$ center absorbs around 325 nm and the F_3-center should be near 300 nm in absorption. This strengthens the tentative assignments made earlier in this study.

TABLE I

COMPARISON OF PREDICTED AND EXPERIMENTAL VALUES OF F-AGGREGATE CENTER ABSORPTION IN SELECTED CRYSTALS

Material	F_2-Center		F_3-Center		F_3^+-Center	
	Exp	Pred	Exp	Pred	Exp	Pred
LiF						
d=2.83Å ε=2.20	444 nm	445 nm	391 nm	414 nm	487 nm	455 nm
NaF						
d=3.27Å ε=2.20	499 nm	501 nm	450 nm	458 nm	546 nm	627 nm
$KMgF_3$						
d=2.81Å ε=2.20	445 nm	446 nm	396 nm	412 nm		460 nm
MgF_2						
ε=a.83						
d=2.576Å (D_{2h})	322 nm	329 nm	300 nm	303 nm		
d=2.813Å (C_1)	355 nm	355 nm				444 nm
d=3.342Å (C_{2h})	370 nm	370 nm				

CHAPTER V

TRANSITIONS IN NICKEL-DOPED MgF_2 AND MnF_2

In this chapter the results of our investigation into the nickel transition of doped crystals of MgF_2 and MnF_2 is presented. The study looks most closely at the infrared transition, $^3T_{2g} \rightarrow {}^3A_{2g}$, in both crystals, examining the excitation spectra, the temperature dependence of the lifetime, and the effects of electron irradiation upon this transition. In addition, analysis of the temperature dependence of the lifetime in MgF_2 for the transitions $^3T_{2g} \rightarrow {}^3A_{2g}$ and $^1T_{2g} \rightarrow {}^3T_{2g}$ allows us to develop a rather compete configuration coordinate diagram for the Ni^{2+} ion in MgF_2. Then, a look at the energy transfer between the Mn^{2+} ions of an MnF_2 host and the Ni^{2+} dopant ions gives some perspective on efficiency levels of lasers using these host materials. Finally, the radiation damage of these materials is studied.

MgF_2:Ni

The emission spectra of the $^3T_{2g} \rightarrow {}^3A_{2g}$ transition of Ni^{2+} in MgF_2 is displayed in Figure 15. This figure shows the change in the emission spectra between 15 K and 77 K. An excitation spectra of this same transition at 15 K is shown in Figure 16, along with the absorption spectrum. Notice how the excitation spectrum mirrors the

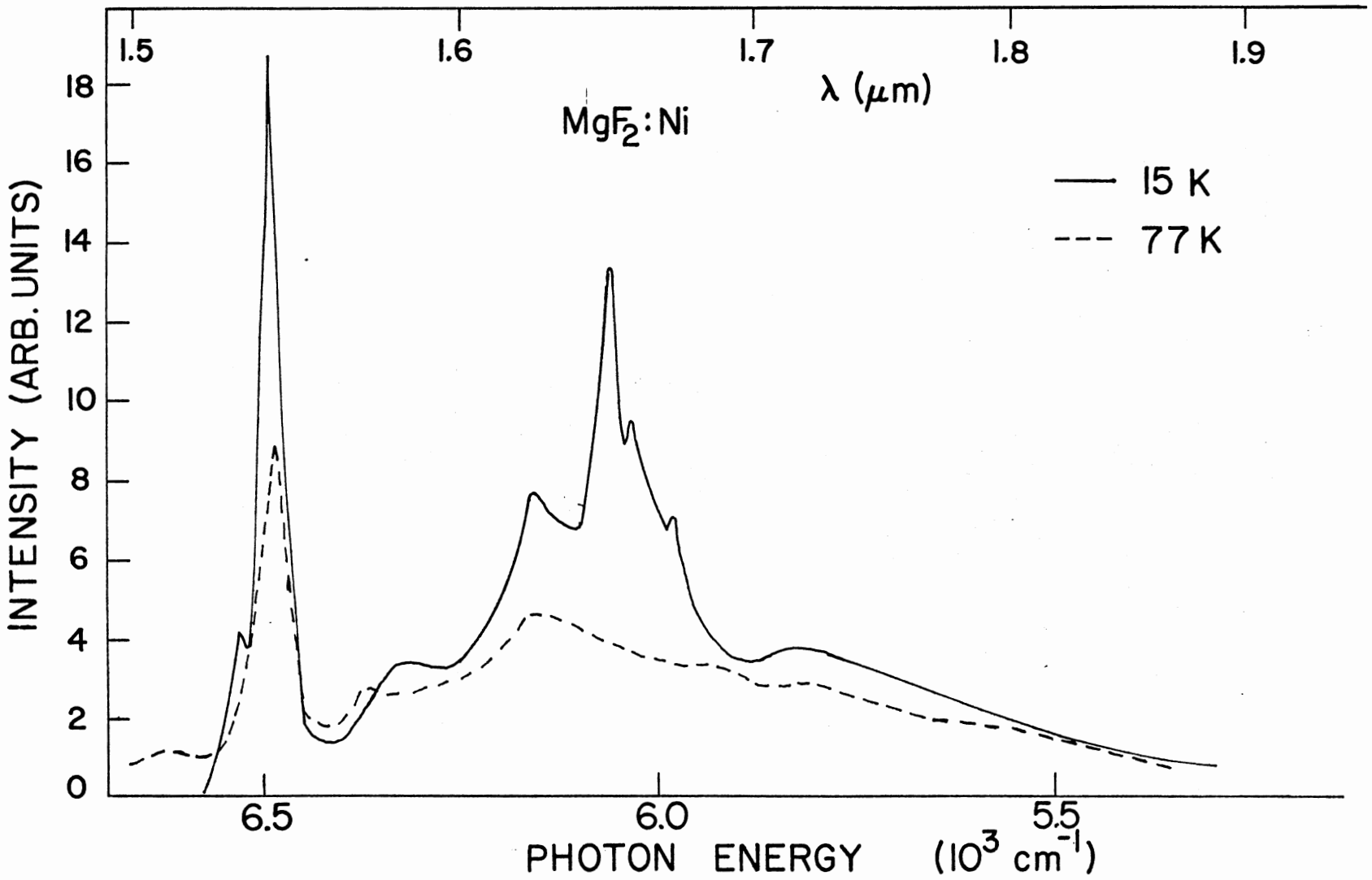

Figure 15: Infrared Emission Spectra for Ni^{2+} in MgF_2 at 15 K and 77 K

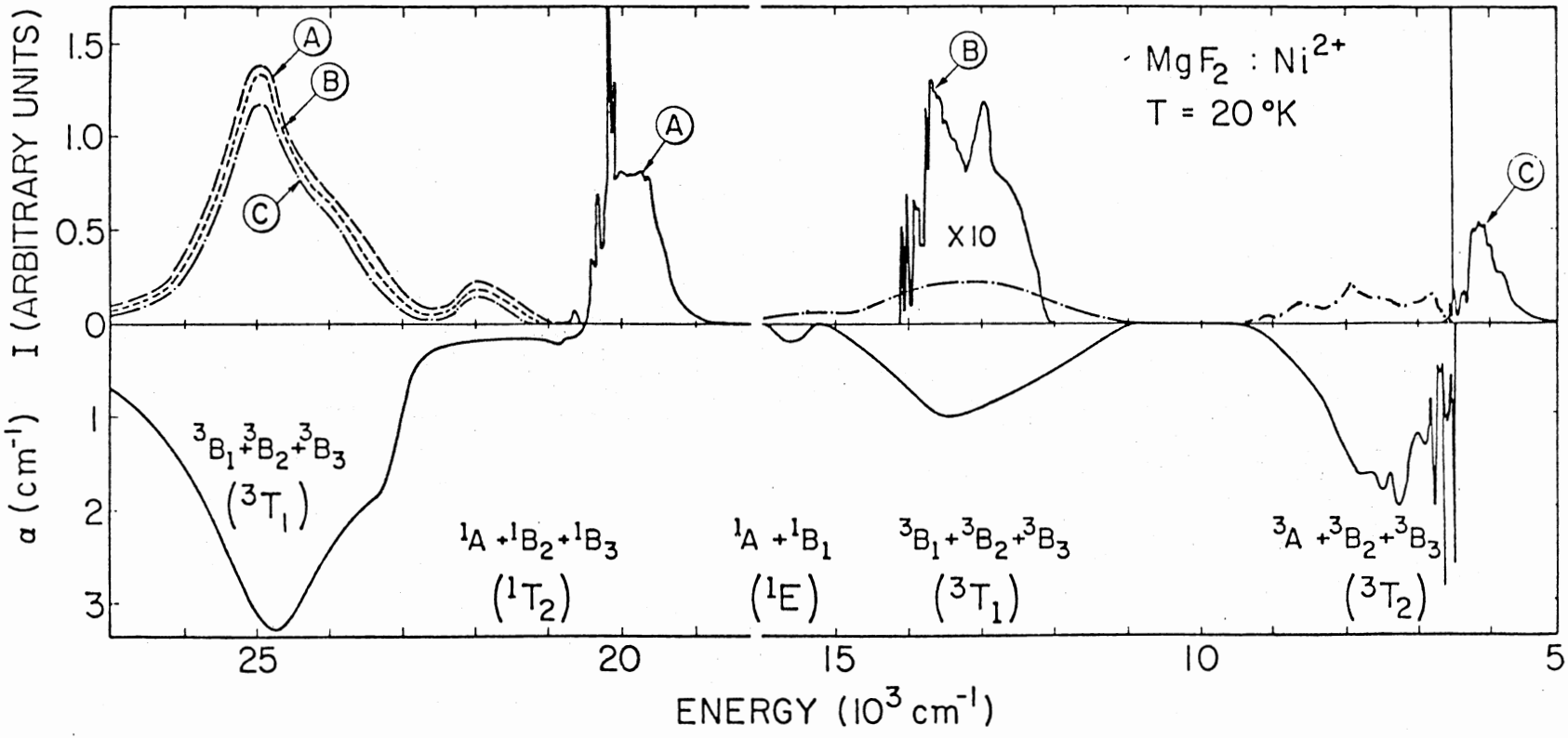

Figure 16: Excitation and Absorption Spectra for Ni^{2+} in MgF_2 at 15 K

absorption spectrum, indicating the feeding of the $^3T_{2g}$ level from high energy levels of the ion. Also very prominent in the emission spectrum is the zero phonon line at 6492 cm^{-1}(1.54 m). Previous work (48,49) has centered on transitions in the visible wavelength region, giving evidence that the red emission (1400 cm^{-1}) and the green emission (200,000 cm^{-1}) both arise from the $^1T_{2g}$ level. Evidence this centers around the identical temperature dependence of the two transitions; transitions arising from different levels would not likely have identical temperature dependences.

The temperature dependence for these three transitions in MgF_2:Ni is shown in Figure 17. The data for the IR transition was published by Moulton and Mooradian (47) and verified by these experiments. The data for the red and green transitions was collected and published by Iverson (48). These data were also checked for consistency.

In the figure, the fits generated by a Struck and Fonger analysis are shown as solid lines. Parameters found to give the best fit are shown in Table II, and perhaps significantly the dominant phonon energy is found to be about 250 cm^{-1} in both cases. These parameters were then used to construct the configuration coordinate diagram shown in Figure 18.

MnF_2:Ni

Figures 19 and 20 shown the infrared emission spectrum and the excitation/absorption spectra for MnF_2:Ni at 15 k. Noticeable in comparison with the MgF_2:Ni spectra are several features. First, the emission is shifted to lower energy in the MnF_2 host, the $^3T_{2g} \rightarrow {}^3A_{2g}$ zero phonon line being at 5927 cm^{-1} as opposed to 6492 cm^{-1}. Likewise,

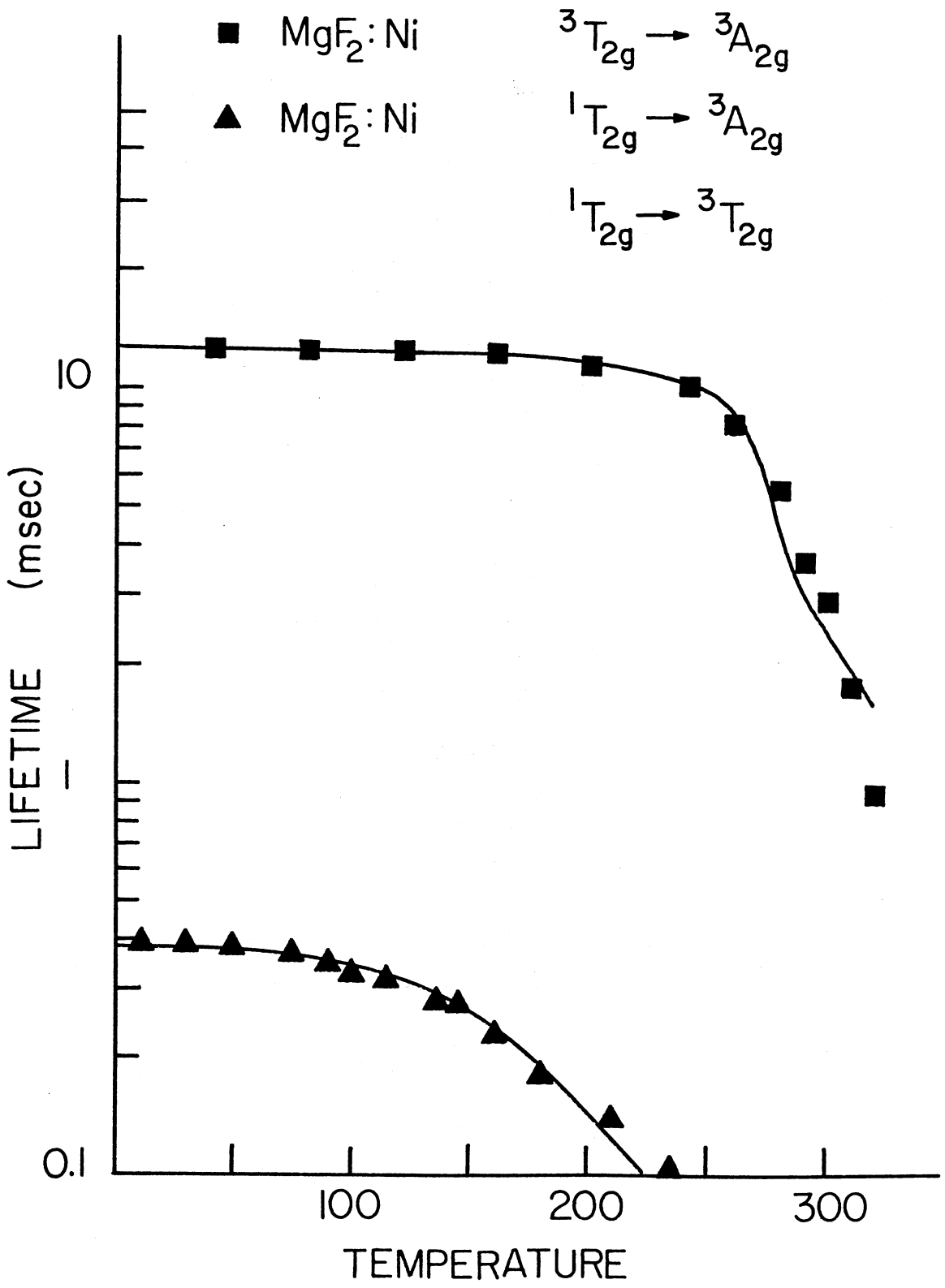

Figure 17: Temperature Dependence of the Lifetimes of Ni^{2+} Transitions in MgF_2

TABLE II

STRUCK AND FONGER PARAMETERS FOR MgF_2:Ni

Parameter	$^3T_{2g} \rightarrow {}^3A_{2g}$	$^1T_{2g} \rightarrow {}^3T_{2g}$
A_{uv}	3.61	3.20
p_U	26	19
$h\omega_v$	24.8 cm^{-1}	250 cm^{-1}
θ	44.85^o	45^o
N_{uv}	$1x10^{13}$	$1x10^{13}$
τ_o	11.4 msec	430 μsec
zero phonon energy	6448 cm^{-1}	4750 cm^{-1}
absorption maximum	7251 cm^{-1}	
emission maximum	5644 cm^{-1}	

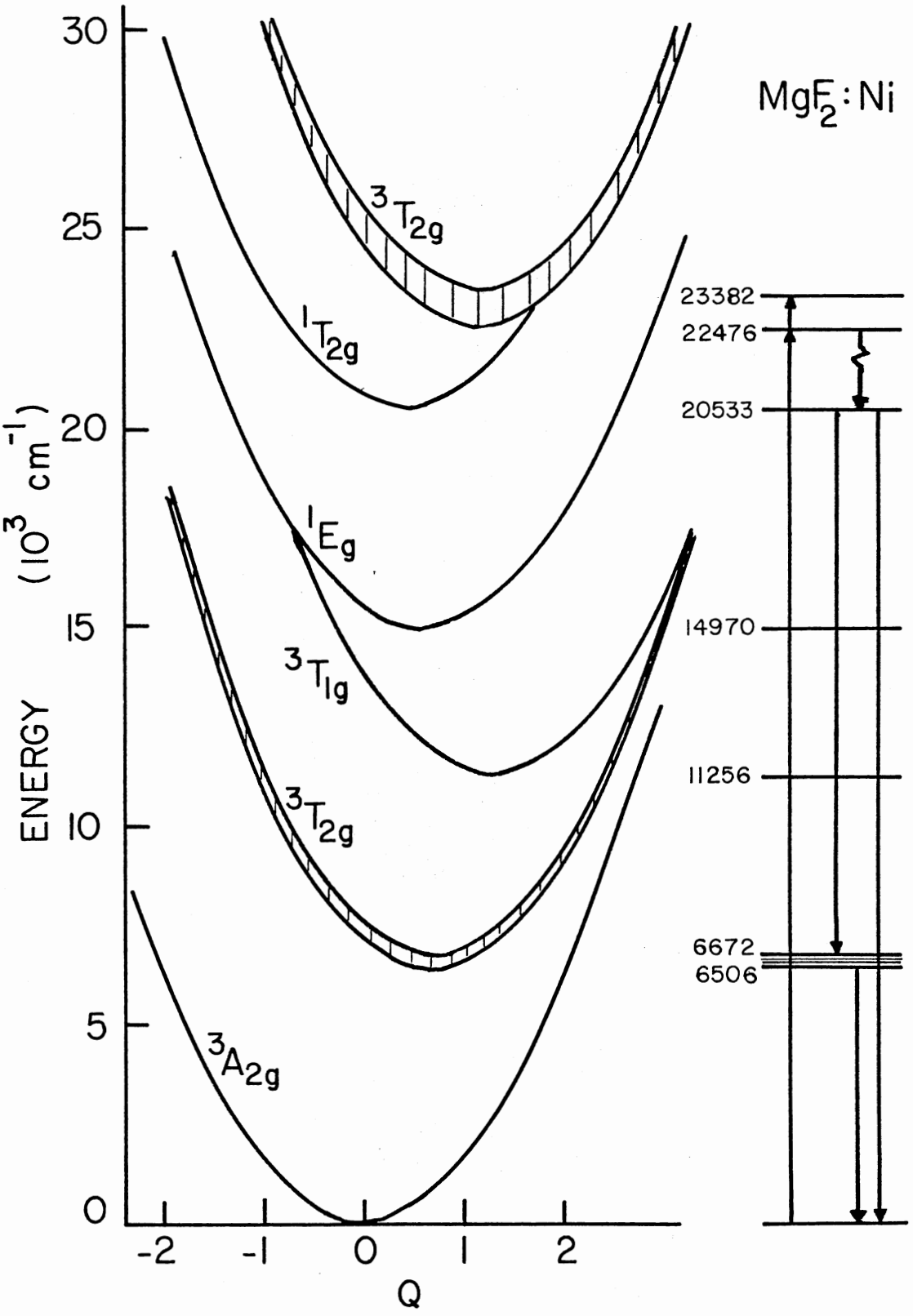

Figure 18: Configuration Coordinate Diagram for Ni^{2+} in MgF_2 Based on the Struck and Fonger Analysis

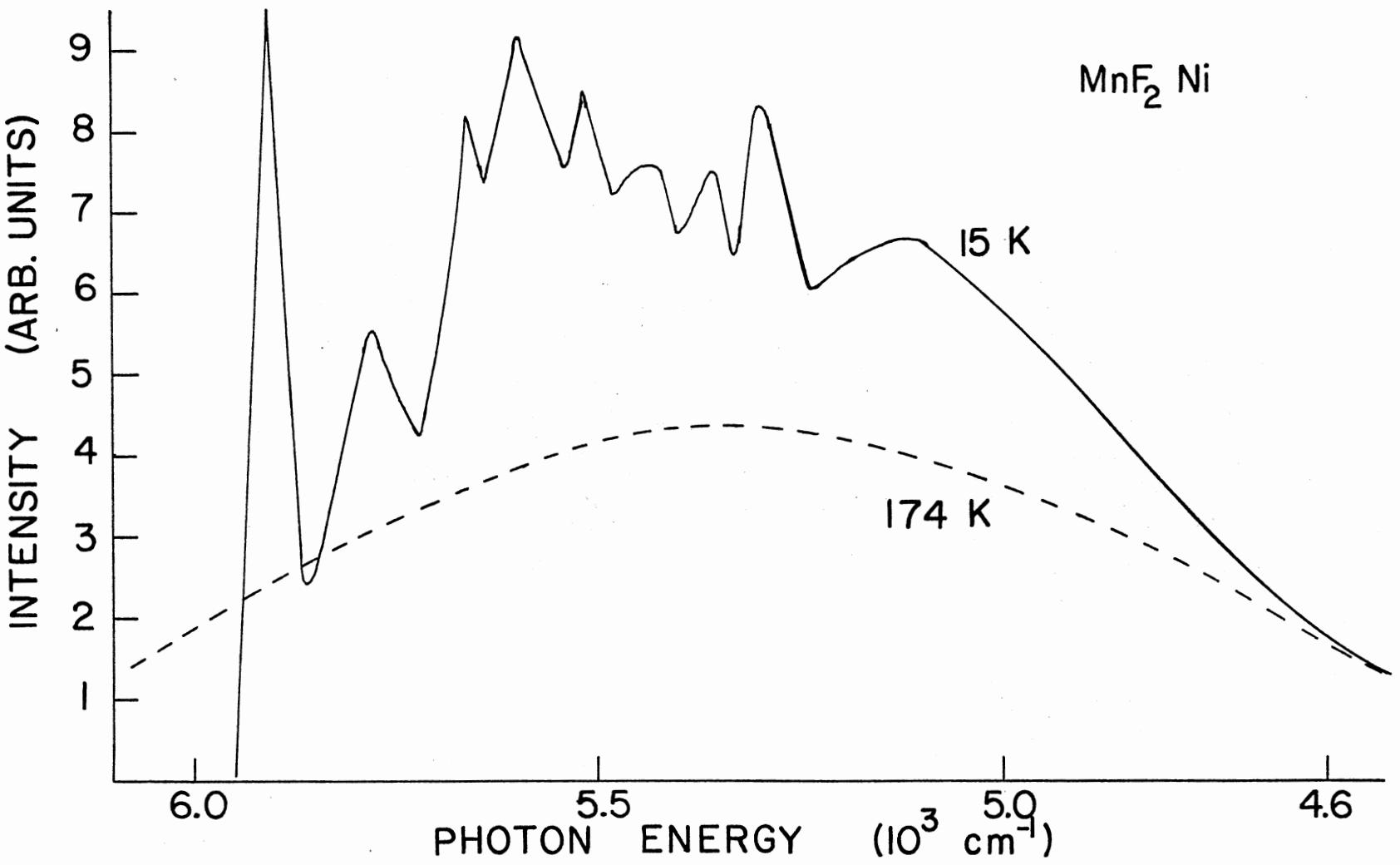

Figure 19: Infrared Emission Spectrum for Ni^{2+} in MnF_2 at 15 K

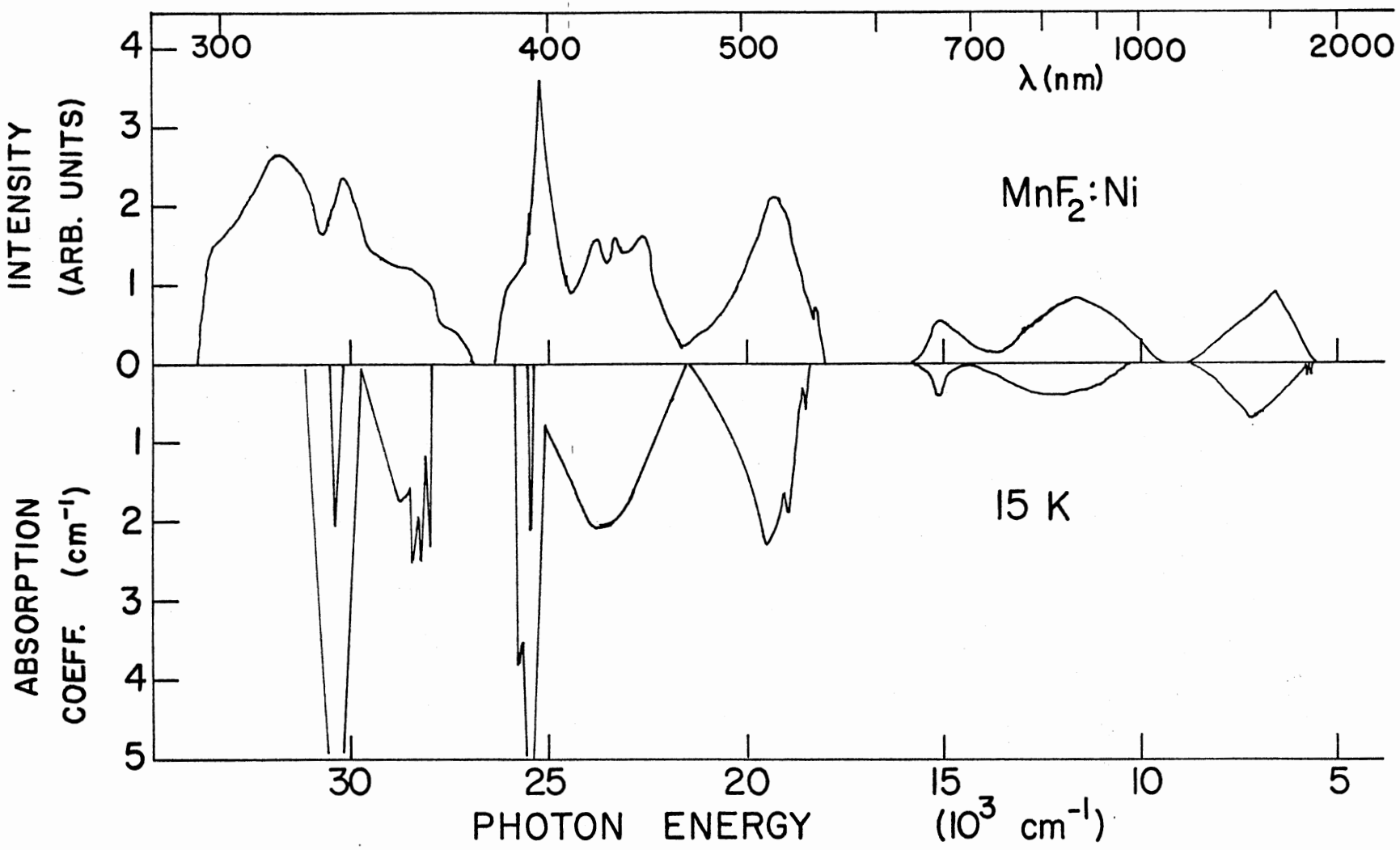

Figure 20: Excitation and Absorption Spectra for MnF_2:Ni at 15 K

the broad band maximum is shifted to lower energy. Secondly, several sharp peaks in the spectra, occuring at 5804 cm^{-1} and 5672 cm^{-1}, have been identified as zero phonon lines caused by the splitting of the $^3A_{2g}$ ground state by the antiferromagnetic MnF_2 lattice (4). Thirdly, the excitation spectrum reflects the energy transfer from the Mn^{2+} ions of the host lattice to the Ni^{2+} ions, and their subsequent radiative decay from $^3T_{2g}$ to the ground state. In particular, the $^1T_{2g}$ level of the Ni^{2+} ions appears toally buried beneath the $^4T_{1g}$ level of the Mn^{2+} ions. As in the emission spectra, the energy levels of the excitation spectrum are all shifted to lower energy levels than in MgF_2:Ni.

The temperature dependence of the $^3T_{2g} \rightarrow {}^3A_{2g}$ transition in MnF_2:Ni is shown in Figure 21. Although the lifetime at low temperature is very comparable to the cooresponding lifetime in MgF_2:Ni, the temperature dependence is much stronger, the lifetime being down a factor of two by 150 K. The Struck and Fonger analysis was performed on this transition also, with parameters being as follows:

$\theta = 45^o$, $\hbar\omega = 260\ cm^{-1}$, $A_{uv} = 3.35$, $p_U = 21$, and $\tau_o^{``} = 16$ msec, N_{uv} was fixed at $1x10^{13}$.

An attempt was made to study the visible transitions in MnF_2:Ni, in particular the lifetime of the $^1T_{2g}$ to $^3T_{2g}$ transition of Ni^{2+}. An unirradiated sample was examined, but the intensity of luminescence was extremely low, making the identification of transitions more difficult. A transition tentatively identified as the $^1T_{2g} \rightarrow {}^3A_{2g}$ was noted at about 18,500 cm^{-1}, having a lifetime at 15 K of about 150 msec. The intensity of this band is strongly temperature dependent, having diminished by 100 K. No indication of the weaker,

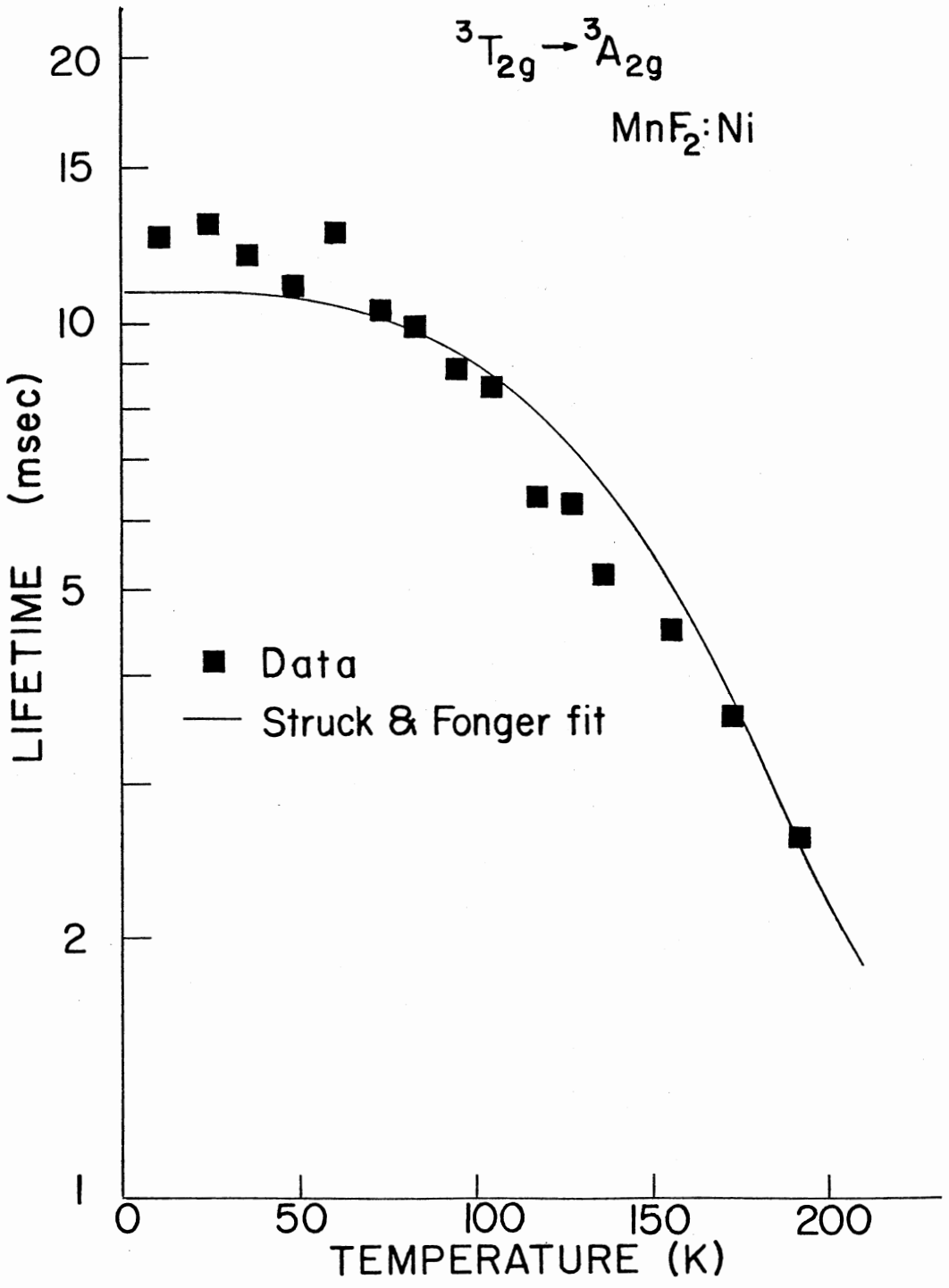

Figure 21: Temperature Dependence of the Lifetime of $^3T_{2g} \rightarrow {}^3A_{2g}$ Transition in MnF_2:Ni

$^1T_{2g} \rightarrow {}^3T_{2g}$ transition was noted, but there is some possibility that the sensitivity of the EMI 9659 PMT might be low enough in the region where this band is expected that it would not be observed.

It also appeart that the Mn^{2+} transitions normally seen around 18,000 cm^{-1} are significantly inhibited by the presence of the nickel impurity. Comparison of the doped MnF_2 crystal with "pure" MnF_2 indicated that the Mn^{2+}luminescence is reduced by a factor of roughly 10^3 due to the nickel. This is most likely due to the Mn_{2+} ion transferring energy to the nickel ion, rather than making a radiative transition to the ground state.

Energy Transfer

One of the crucial questions that this study seeks to answer concerns energy transfer from the Mn^{2+} lattice to the Ni^{2+} ions. The basic question is, can a larger portion of radiant energy incident on the laser crystal be transferred to the lasing transition in MnF_2 is the host rather than MgF_2? The choice of MnF_2 as host is based on the high absorption coefficients of the Mn^{2+} ions in the region from 300 nm to 500 nm, and the strong energy overlap of the $^4T_{1g}$ manganese band with the $^1T_{2g}$ band of nickel. This overlap presents strong possibilities for resonant energy transfer.

If such an enhancement of the laser output is obtainable by a change in the host, a nickel laser excited by a broad band source such as a xenon lamp would have greater overall efficiency in the MnF_2 host as opposed to the MgF_2 host.

A comparison of the excitation spectra for the $^3T_{2g} \rightarrow {}^3A_{2g}$ IR transition in nickel-doped MgF_2 and MnF_2 is shown in Figure 22.

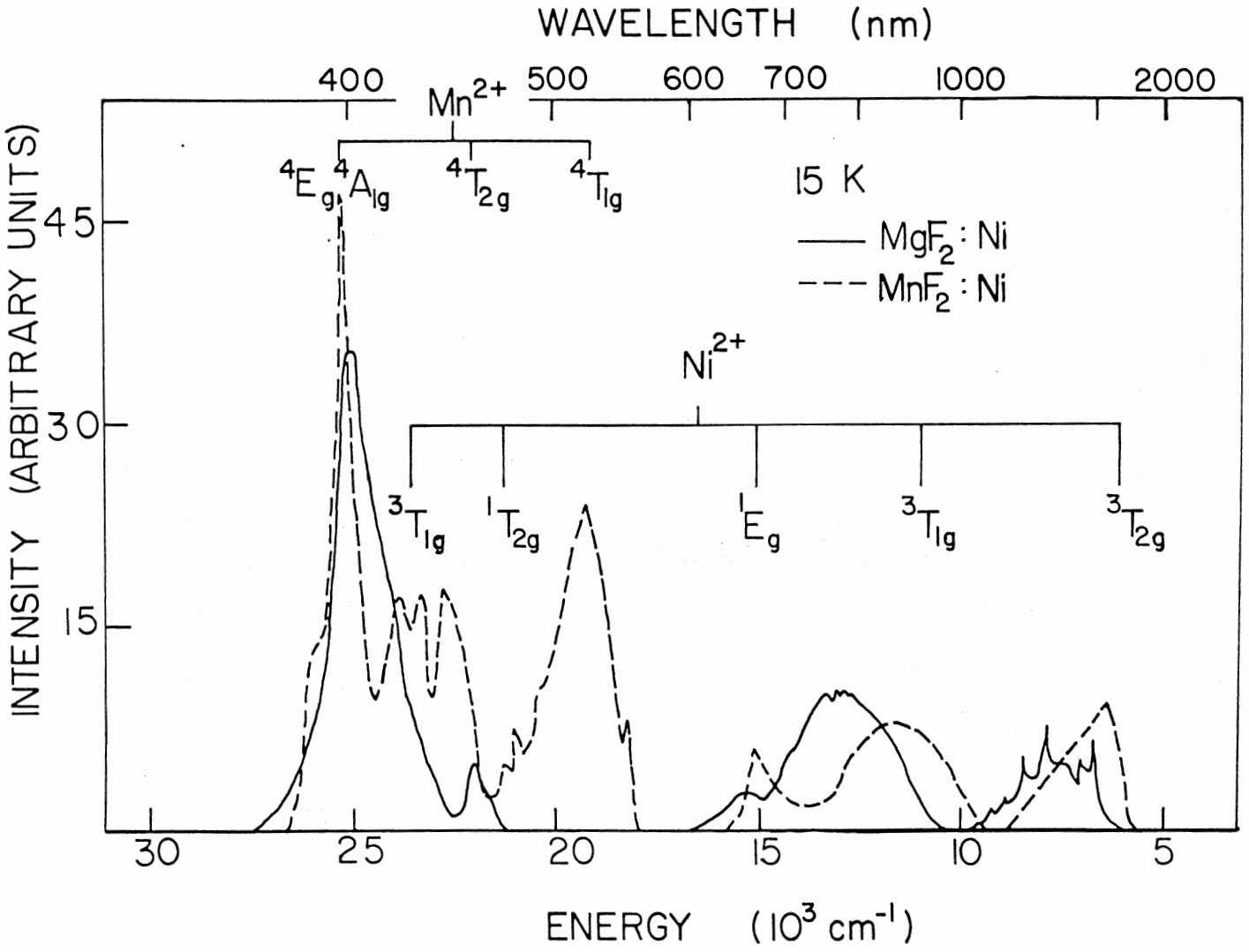

Figure 22: Excitation Spectra for MgF_2:Ni and MnF_2:Ni at 15 K

Corrections have been made for the spectral output of the lamp, the optical system, and the difference in concentration of the nickel impurity in the two crystals used. The approximate positions of each of the bands is indicated on the diagram.

Several features are immediately noticeable from this diagram. The first is the shift of energy levels to slightly lower energy in MnF_2 as compared with MgF_2. Second, one sees quickly the location of the Mn^{2+} bands in relation to the Ni^{2+} bands, in particular the overlap of $^4T_{1g}$ and $^1T_{2g}$ in the region of 20,000 cm^{-1}. Third, one notices that the ^1E_g, $^3T_{1g}$, and $^3T_{2g}$ bands have roughly the same magnitude in both MnF_2 and MgF_2. Since these are purely nickel bands, dependents upon nickel concentration, such similar magnitude is expected if concentration has been corrected for.

The feature of interest is in the region from 26,000 cm^{-1} to 18,000 cm^{-1}, where the Mn^{2+} bands exist. In this region, the area under the excitation curve for MnF_2 is 1.96 times as great as that under the curve for MgF_2. This factor of 2 is strong evidence of energy transfer. Further, it is obvious that the $^1T_{2g}$ band in MgF_2 is fairlysmall compared with the $^3T_{1g}$ band. In MnF_2, the resonant energy transfer feeds this band, and causes this region to be much greater in magnitude than the nickel transition alone could ever be. Thus, a laser stimulated by light in the region near 20,000 cm^{-1} (500 nm) could be enhanced about 15 times by the energy transfer of the $^4T_{1g}$ level as compared to just the $^1T_{2g}$ level alone.

Radiation Damage

An important question for solid state lasers, especially those with infrared transitions, is, how much does radiation degrade the performance? The relevance of this question is due to the possibility of satellite operation on these lasers in a communications role, where exposure to the Van Allen belts implies possible radiation damage. Thus, this study involved electron irradiation of the crystals with 1.7 MeV electrons to observe possible radiation-induced changes in the transition.

The MgF_2:Ni crystal, irradiated at room temperature with about 10^{15} electrons per cm^2, was studied for any noticeable changes in both the emission spectra and the excitation spectra of the infrared transition. No change in the excitation spectra was detected, leading one to conclude that no significant changes in oscillator strength of any of the nickel transitions in this crystal occurs. Had such a change in oscillator strength occured, noticeable enhancements or dimunitions of intensity in excitation would be found. The emission spectra was checked for any shift in emission energy, indicating that a vacancy (F-center) near the nickel ion had perturbed the nickel transitions. Again, the lack of any noticeable perturbation indicates that the nickel transition probably does not act as a "trap" for F-centers, and consequently it is not likely to be significantly affefted by radiation damage. A further check was made to see if the lifetime of the transition was changed. Again, the lifetime is related to the oscillator strength of the transition, and any enhancement of oscillator strength would be reflected in a shorter lifetime. No change was noted, again supporting insensitivity of the

nickel transition to radiation.

An MnF_2:Ni sample was irradiated at 77 K by 1.7 MeV electrons, receiving a dose of about $7x10^{14}$ electrons/cm^2. The lifetime of the IR emission ($^3T_{2g} \rightarrow {}^3A_{2g}$) was checked for any change, and seemed to be unaffected. Likewise, the excitation and emission spectra for this IR transition were unaffected, just as with the MgF_2:Ni crystal. However, a new band, as shown in Figure 23, in the visible region at about 15,900 cm^{-1} (630 nm) was observed, which seemed to be the radiation-induced band previously reported in pure MgF_2. Examination of the excitation spectra, especially the polarization of the excitation, confirmed that this was indeed the same band. The temperature dependence of the lifetime of this band was measured, and is shown in Figure 24.

Figure 25 shows a comparison of the excitation and emission of the radiation-induced band with the corresponding spectra of the Ni^{2+} band ($^3T_{2g} \rightarrow {}^3A_{2g}$). It is important to note that the Mn^{2+} bands that excite the 15,900 cm^{-1} radiation band are all perturbed, shifted to lower energy compared to the unirradiated crystal. This shifting indicated that the resonance condition for energy transfer from the $^4T_{1g}$ band of Mn^{2+} to $^1T_{2g}$ level of Ni^{2+} is no longer satisfied for radiation-perturbed Mn^{2+} ions. Thus, the energy absorbed by perturbed Mn^{2+} ions is not transferred to the Ni^{2+} ions, but rather is radiatively emitted as the Mn^{2+} ions return to the ground state directly. Since the concentration of such perturbed Mn^{2+} ions is rather small, the intensity of the Ni^{2+} remains essentially the same, because the number of Mn^{2+} ions which are not perturbed is roughly constant.

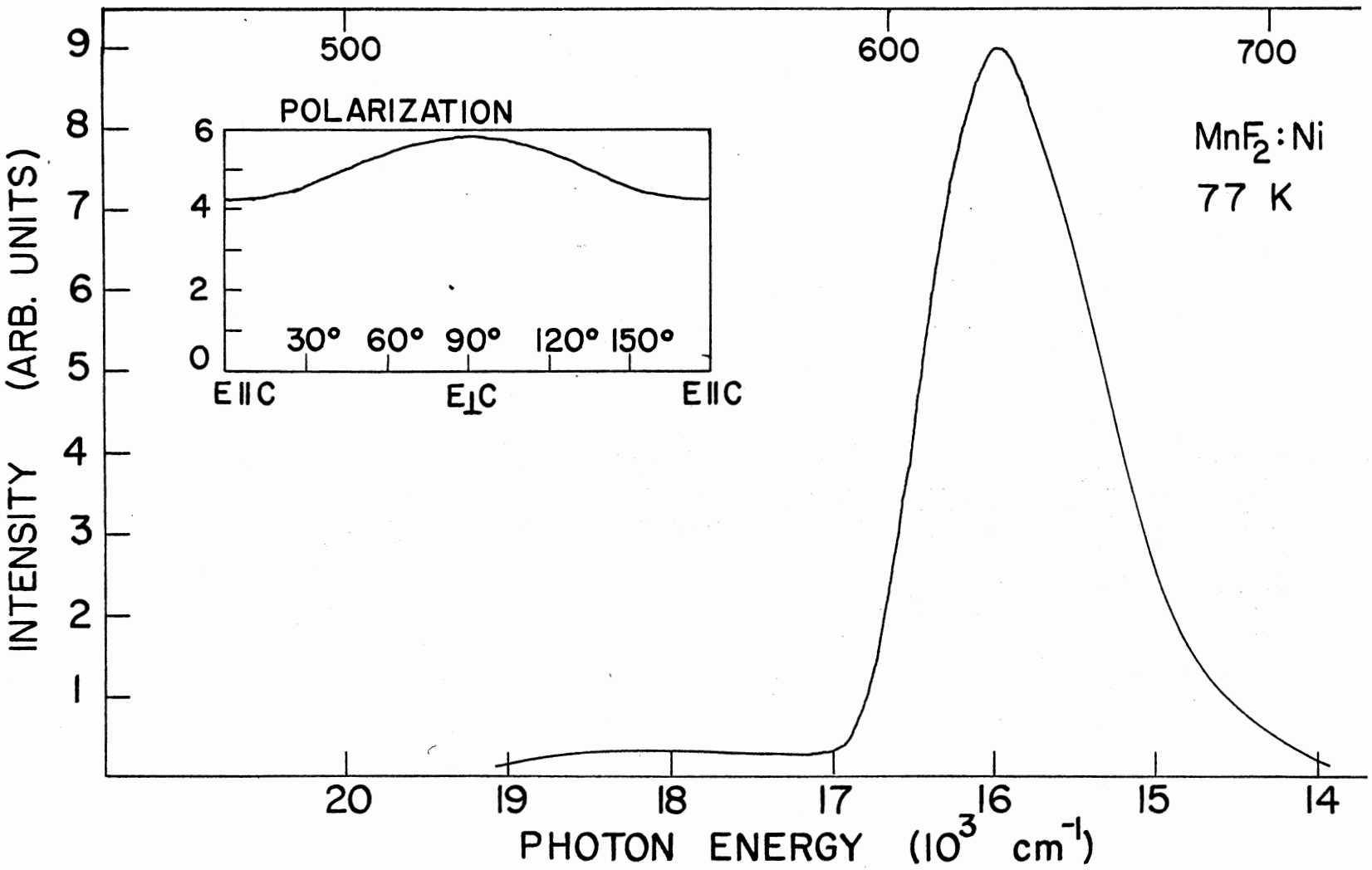

Figure 23: Radiation-Induced Emission Band in MnF_2:Ni

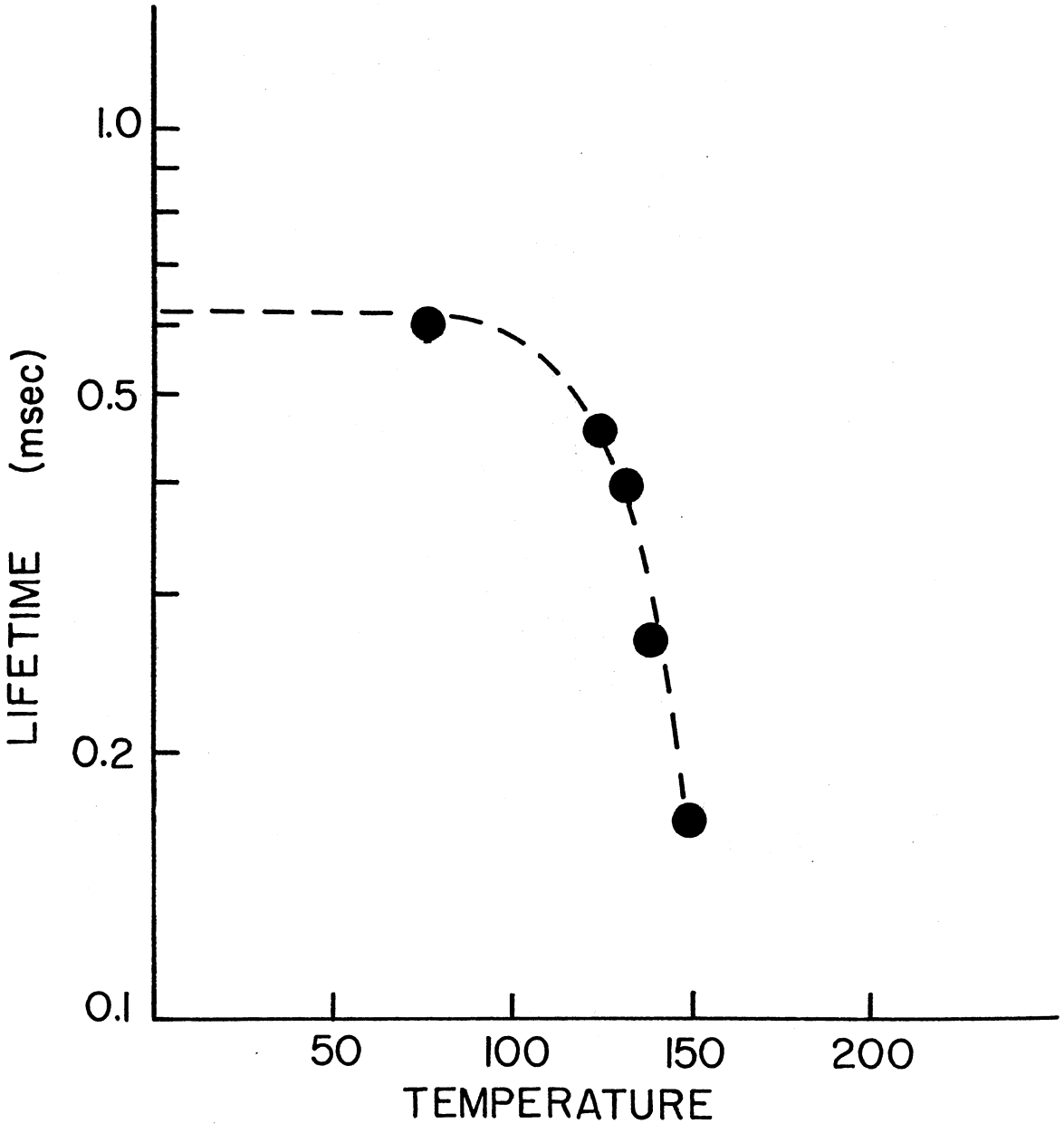

Figure 24: Temperature Dependence of the Lifetime of 630 nm Band in Irradiated MnF_2:Ni

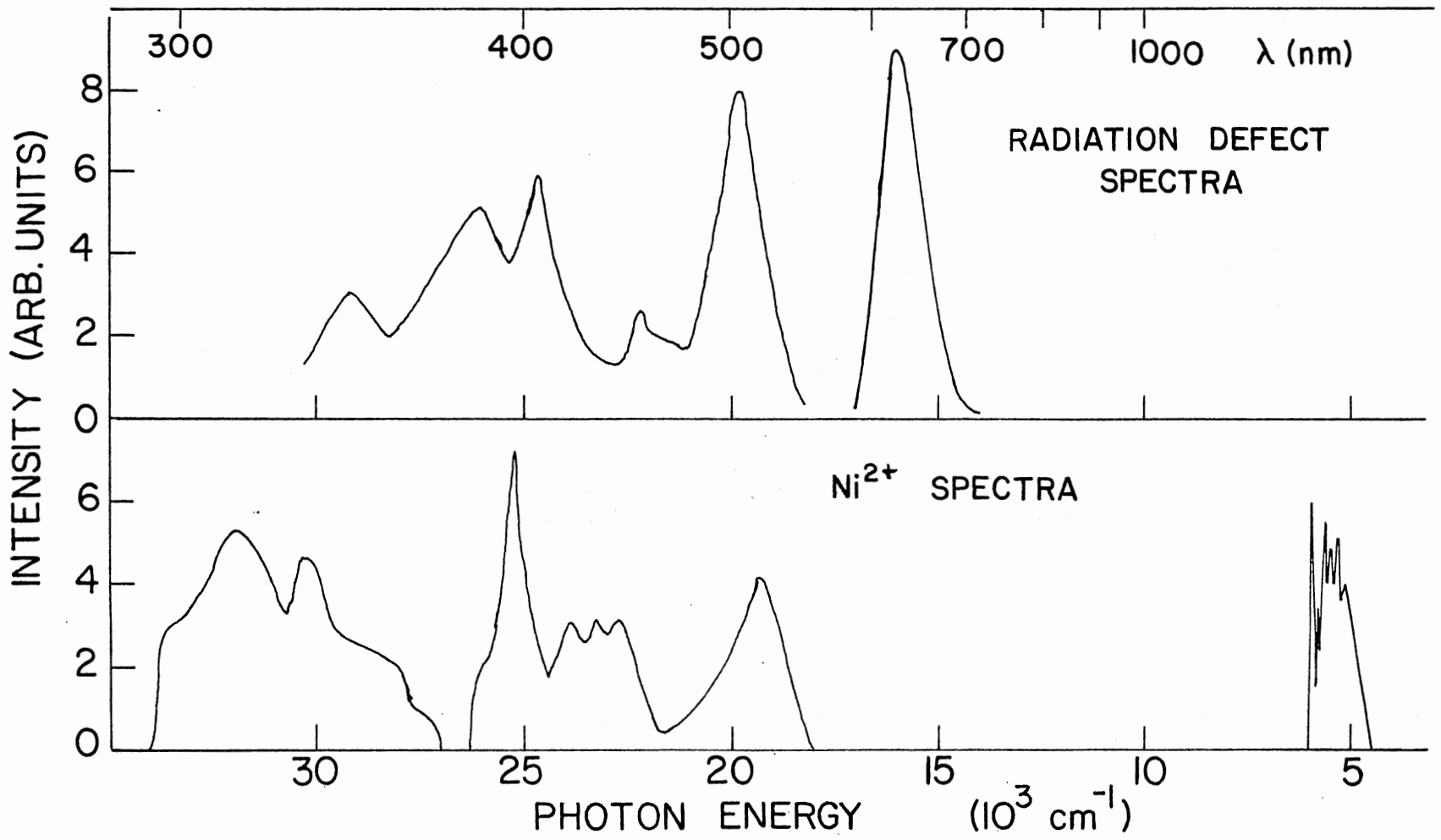

Figure 25: Comparison of Excitation and Emission Spectra in MnF_2 for Ni^{2+} Emission and Radiation perturbed Mn^{2+} Emission

We are able to see then that radiation, at least to doses on the order of 10^{15} electrons/cm^2, do not appreciably affect the characteristics of the Ni^{2+} transition ($^3T_{2g} \rightarrow {}^3A_{2g}$).

CHAPTER VI

SUMMARY AND SUGGESTIONS FOR FURTHER STUDY

We see from the preceding discussion that assignments for several absorption and emission bands that appear in irradiated pure MgF_2. As these bands are significantly enhanced during a period of "bleaching", as the F-band is diminished, the conclusions are that these bands are likely due to F-aggregate centers. The assignments are based on the model of the hydrogen molecule and hydrogen molecular ion, with polarization studies lending additional support.

These assignments in pure MgF_2 and the $F_2(C_1)$ center is an unpolarized band observed to absorb light of 360 nm (27,800 cm^{-1}). The $F_2(C_{2h})$ center and $F_2(D_2)$ center are as previously identified (22, 24), and the F_3 center is identified as absorbing light of 300 nm (33,300 cm^{-1}) with no observed emission. The absorption is polarized $E \perp C$, indicating that the F_3 center probably consists of two adjacent fluorine vacancies in one layer bound with another vacancy in the next layer. This is a reasonable possibility for the F_3 center, and would bear out the observed polarization of the center. No identification is made for the 400 nm (25,000 cm^{-1}) absorption band and the associated 600 nm (16,700 cm^{-1}) emission band, which have previously been identified as the $F_2(C_1)$ band.

Some work that remains to be done on these centers is to measure the lifetime and study the temperature dependence of those lifetimes, so that analysis similar to that done in the Struck and Fonger program could be done. Additionally, some ESR studies may be in order, to more positively identify each of the centers. While ESR is difficult for the F_2 centers, because they are singlet in the ground state, the triplet excited state could be studied. These studies could confirm the assignments made, which are more important as the list of applications of MgF_2 grows.

The laser crystal MgF_2:Ni has been studied by examining its absorption, emission and excitation spectra of the the nickel transitions. The temperature dependence of the lifetimes of the transitions $^1T_{2g} \rightarrow {}^3A_{2g}$ have been analyzed with the Struck and Fonger multiphonon decay technique, and a complete configuration coordinate diagram based on this analysis has been presented. The analysis indicates a dominant phonon energy of about 250 cm^{-1} for both transitions, and Huang-Rhys values of 2.56 and 3.25 respectively. These correspond reasonably well with the anticipated values of this parameter.

Irradiation of this crystal by 1.7 MeV electrons does not affect the lasting transition in either emission energy or lifetime. Therefore, it is likely the crystal is impervious to radiation damage, and may be used in a radiation-filled environment without significant degradation of its performance.

The nickel transitions in MnF_2:Ni have been similarly studied, with special emphasis on the possibility of energy transfer from Mn^{2+} ions to the Ni^{2+}as a means of enhancing the output of the lasting nickel transition. The nickel transitions in this crystal are all

shifted to somewhat lower energies, and the lifetime of the IR transition ($^3T_{2g} \rightarrow {}^3A_{2g}$) shown much greater temperature dependence than was observed in MgF_2:Ni. The Struck and Fonger analysis was applied to the $^3T_{2g} \rightarrow {}^3A_{2g}$ transition, but other, higher energy transitions were too weak to study in detail.

The energy transfer study indicated that the $^4T_{1g}$ level of Mn^{2+} strongly overlapped the $^1T_{2g}$ level of Ni^{2+}, resulting in resonant energy transfer to the nickel ion. This resulted in an enhancement of output of the $^3T_{2g} \rightarrow {}^3A_{2g}$ transition by a factor of 2 when the exciting light was in the visible region.

Radiation damage by 1.7 MeV electrons again appeared to have no effect on the $^3T_{2g} \rightarrow {}^3A_{2g}$ nickel transition, but did induce a transition previously attributed to perturbed Mn^{2+} ions. Study of the excitation spectra confirmed this, and also indicated that the perturbed $^4T_{1g}$ energy level was shifted enough to lower energy that the resonant energy transfer no longer occured. This indicates that radiation could degrade the enhancement of nickel transitions that resulted from such energy transfer.

Further study needs to be conducted on other 3-d ions such as cobalt, chromium, iron, and vanadium in the rutile host material. Preliminary work done in conjunction with this work on cobalt-doped MgF_2 and MnF_2 indicate that radiation effects are more significant in these materials, but technical problems with the detection system curtailed these efforts temporarily. The possibility that one of these crystals may provide a more efficient laser, or that it might have a significantly reduced temperature dependence, makes this search important for those interested in immediate applications. Further

studies might also examine the potential of these crystals as upconverters. Such material would have tremendous technological impact in devices such as night vision optics and as coating on low-power consumption, IR-emitting Light Emitting Diodes, to make their output visible while keeping power consumption minimal.

BIBLIOGRAPHY

1. Sibley, W. A., & D. Pooley, in Treatise on Material Science and Technology, edited by H. Hermann (Academic Press, New York, 1947), p. 46.

2. Brice, J. C., The Growth of Crystals From the Melt (North Holland Publ. Co., Amsterdam), 1965.

3. Bullington, D. S., & J. H. Crawford, Jr., Radiation Damage in Solids (Princeton University Press, Princeton, NJ), 1961.

4. van Doorn, C. Z., Rev. of Sci. Instr., 32, 755 (1961).

5. Seitz, F., Rev. Mod. Phys., 18, 384 (1946).

6. Seitz, F., Rev. Mod. Phys., 26, (1954).

7. Kittel, C., Intro. to Solid State Physics, 4th ed. (Wiley, New York, 1971),p. 611.

8. Mooradian, A., Rep. Prog. Phys., 42, 1533 (1979).

9. Bishop, H. E., R. P. Henderson, P. Irdale, & D. Pooley, Appl. Phys. Lett., 20, 504 (1972).

10. Sibley, W. A. & E. Sonder, J. Appl. Phys., 34, 2366 (1963).

11. Caro, P. & P. Porcher, J. Lum., 18/19, 257 (1979).

12. Watts, R. K. & W. C. Holton, Solid State Comm., 9, 137 (1970).

13. de Boer, J. H., Rec. Trav. Chim. Pays-Bas, 56, 301 (1937).

14. van Doorn, C. Z., Philips Res. Rep. Suppl. No. 4 (1962).

15. Compton, W. D. & H. Rabin, Solid State Physics, 16, 121 (1965).

16. Markham, J. J., in Solid State Physics, edited by F. Seitz and D. Turnbull (Academic Press, New York, 1966), Suppl. No. 8.

17. Schulman, J. H., & W. D. Compton, Color Centers in Solids (MacMillan Co., New York, 1962).

18. Fowler, W. B., in Physics of Color Centers, edited by W. B. Fowler (Academic Press, New York, 1968), p. 54.

19. Click, C. C., in Point Defects in Solids, edited by J. H. Crawford and L. M. Slifkin (Plenum, New York, 1972) p. 291.

20. Duncanson, A. and R. W. H. Stevenson, Proc. Phys. Soc., 72, 1001 (1958).

21. Hills, M. E., and W. R. McBride, J. Chem. Phys., 40, 2053 (1964).

22. Blunt, R. F., & M. I. Cohen, Phys. Rev., 153, 1031 (1967).

23. Facey, O. E., & W.A. Sibley, Phys. Rev. 174, 1076 (1968).

24. Facey, O. E., & W. A. Sibley, Phys. Rev. B, 2, 1111 (1970.

25. Sibley, W. A., & O. E. Facey, Phys. Rev., 174, 1076 (1968).

26. Mostoller, M., B. Henderson, W. A. Sibley, & R. F. Wood, Phys. Rev. B 4, 2667 (1971).

27. Mostoller, M., B. N. Ganguly, & R. F. Wood, Phys. Rev. B 4, 2015 (1971).

28. Fitchen, D. B., in The Physics of Color Centers, edited by W. B. Fowler (Acedemic, New York, 1968).

29. Klick, C. C.,& J. H. Schulman, Solid State Physics, 5, (1957).

30. Aegerter, M. A., & F. Luty, Phys. Status Solidi B 43, 245 (1971).

31. Herman, R., M. C. Wallis, & R. F. Wallis, Phys. Rev., 103, 87 (1956).

32. Mulliken, R. S., Rev. Mod. Phys., 4, 1 (1932).

33. Slater, J. C., Quantum Theory of Molecules and Solids (McGraw Hill, New York, 1963) ,Vol. I., p. 67.

34. Present, R. D., J. Chem. Phys., 3, 122 (1935).

35. Bates, D. R., K. Ledshan, & A. L. Stewart, Trans. Roy. Soc. (London), A246, 215 (1953).

36. Coulson, C. A., Proc. Camb. Phil. Soc., 34, 204 (1938).

37. James, H. M., & A. S. Coolidge, J. Chem. Phys., 1, 825 (1933).

38. Podinsh, A. & W. A. Sibley, Phys. Rev. B, 18, 5921 (1978).

39. Blunt, R. F., J. Chem. Phys., 44, 2317 (1966).

40. Johnson, L. F., R. E. Dietz, & H. J. Guggenheim, Phys. Rev. Lett., 17, 13 (1966).

41. Greene, R. L., D. D. Sell, R. S. Feigelson, G. F. Imbusch, & H. J. Guggenheim, Phys. Rev., 171, 600 (1968).

42. Kappers, L. A., S. I. Yun, & W. A. Sibley, Phys. Rev. Lett., 29, 943 (1972).

43. Lee, K. H. & W. A. Sibley, Phys. Rev. b, 12, 3392 (1975).

44. Kim, K. K. & A. S. Nowick, J. Phys. C, 10, 509 (1977).

45. James, R. & C. R. A. Catlow, J. Phys. C., 10, L237 (1977).

46. Ershov, N. N., G. M. Zakkarov, T. O. Nikitinskaya, N. M. Nikulin, & V. M. Reiterov, Opt. Spectrosc (USSR) 44 (4), 432 (1977).

47. Moulton, P. F., & A. Mooradian, Solid State Res. Report, Lincoln Lab., MIT (1978:1), A10.

48. Iverson, M. A. & W. A. Sibley, J. Lum., 20, 311 (1979).

49. Vehse, W. E., K. H. Lee, S. I. Yun, & W. A. Sibley, J. Lum., 10, 149 (1975).

50. Cotton, F. A., Chemical Applications of Group Theory (Wiley, New York, 1963).

51. Struck, C. W. & W. H. Fonger, J. Lum., 10, 1 (1975).

52. Fonger, W. H. & C. W. Struck, J. Chem. Phys., 60, 1994 (1974).

53. Fonger, W. H. & C. W. Struck, Phys. Rev B, 11, 3251 (1975).

54. Struck, C. W. & W. H. Fonger, J. Lum., 14, 253 (1976).

55. Fonger, W. H. & C. W. Struck, J. Lum., 17, 241 (1978).

56. Watts, R. K., Point Defects in Crystals (Wiley, New York, 1977), p. 2.

57. Tanabe, Y. & Sugano, S., J. Phys. Soc.(Japan),9, 753 (1954).

58. Dexter, D. L., Solid State Phys., 6, 353 (1958).

59. Di Bartolo, B., Optical Interactions in Solids (Wiley, New York, 1968),p. 420.

60. Kiel, A., in: Proc. Third Intern. Conf. Quantum Electronics, Paris, 1963, edited by P. Grivet & N. Bloembergen (Columbia Univ. Press, New York, 1964),p. 765.

61. Huang, K. & A. Rhys, Proc. Roy. Soc. (London),A204, 406 (1950).

62. Flaherty, J. M. & B. DiBartolo, J. Lum., 8, 51 (1973).

63. Weber, M. J., Phys. Rev., 157, 262 (1967).

64. Manneback, C., Physica, 17, 1001 (1951).

65. McLure, D. S., J. Chem. Phys., 36, 2757 (1962).

66. Sturge, M. D., Phys. Rev. B, 8, 6 (1973).

67. Watts, R. K., in Optical Properties of Ions in Solids, edited by B. diBartolo (Plenum Press, New York, 1975), p. 307.

68. Reisfeld, R., Structure and Bonding, 30, 65 (1975).

69. Wright, J. C., in Topics in Applied Physics, edited by F. K. Fong (Springer-Verlag, Berlin, 1976).

70. Reisbery, L. A. & M. J. Weber in Progress in Optics, Vol XIV, edited by E. Wolf (North Holland, Amsterdam, 1976), p. 89.

71. Forster, T., Ann. Phys., 2, 55 (1948).

72. Dexter, D. L., J. Chem. Phys., 21, 836 (1953).

73. Orbach, R. in Conf. Properties of Ions in Crystals (Wiley, New York, 1967), p. 455.

74. Miyadawa, T. & D. L. Dexter, Phys. Rev. B, 1, 2961 (1970).

75. Orbach, R. in Optical Properties of Ions in Solids, edited by B. diBartolo (Plenum Press, New York, 1975).

76. Yun, S. I., PhD Thesis, (Oklahoma State University, 1973).

77. Feuerhelm, L. N., MS Thesis, (Oklahoma State University, 1973).

78. Keil, T. H., Phys. Rev., 140, A601 (1965).

APPENDIX

STRUCK AND FONGER PROGRAM

```
 10  DIM U(20)
 20  DIM W(10)
 30  DIM T(15)
 40  DIM L(15)
 50  DIM Q(15)
 60  DIM A(40,20)
 70  DEG
 80  A=3.61  ! **  VALUE OF Auv  **
 90  H=44.85  !  **  VALUE OF THETA  **
100  P=26  !  **  VALUE OF Pu  **
110  W=245  !  **  VALUE OF hw  **
120  TO=.0114  !  **  VALUE OF TO  **
130  W(4)=1.E13  !  **  VALUE OF Nuv  **
140  B=0  !  PRINT FLAG FOR Auv MATRIX  !  0=NOPRINT, 1=PRINT
150  F1=0  !  **FLAG FOR Pu CHANGE
160  READ G
170  K=35
180  S=15
190  FOR D=1 TO G
200  READ T(D), L(D)
210  NEXT D @ BEEP 500,10
220  FOR N=0 TO 39
230  FOR M=0 TO 19
240  A(N,M)=0
250  NEXT M
260  NEXT N @ BEEP 100,30
270  ! **** INITIALIZATION OF MATRIX
280  A(0,0)=SQR(SIN(2*H)) *EXP(-1/8*A^2*SIN(2*H)^2
290  Y=SIN(2*H)*A/SQR(2)
300  A(1,0)=Y*A(0,0)*SIN(H)
310  A(0,1)=-Y*A(0,0)*COS(H)
320  A(1,1)=Y*A(0,1)*SIN(H)+SIN(2*H)*A(0,0)
330  FOR N=1 to 38
340  A(N+1,0)=1/SQR(N+1)*(COS(2*H)*SQR(N)*A(N-1,0)+Y*SIN(H)*A(N,0)
350  NEXT N @ BEEP 350,10
360  FOR M=1 TO 18
370  A(0,M+1)=1/SQR(M+1)*(-COS(2*H)*SQR(M)*A(0,M-1)-Y*COS(H)*A(0,M))
380  A(1,M+1)=1/SQR(M+1)*(-COS(2*H)*SQR(M)*A(1,M-1)-Y*COS(H)*A(1,M)+
     SIN(2*H)*A(0,M))
390  NEXT M @ BEEP 300,10
```

```
400  ! **** REMAINDER OF MATRIX
410  FOR M=1 TO 19
420  FOR N=1 TO 39
430  A(N+1,M)=1/SQR(N+1)*(COS(2*H)*SQR(N)*A(N-1,M)+Y*SIN(H)*A(N,M)+
     SIN(2*H)*SQR(M)*A(N,M-1))
440  NEXT N @ BEEP 250,15
450  NEXT M @ BEEP 200,10
460  IF B=0 THEN 520
470  FOR N=0 TO K-1
480  DISP N,A(N,0),A(N,1),A(N,2),A(N,3),A(N,4),A(N,5),A(N,6),A(N,7)
490  DISP A(N,8),A(N,9),A(N,10),A(N,11),A(N,12),A(N,13),A(N,14)
500  NEXT N @ BEEP 100,30
510  !  CONVERT TO TEMP UNITS
520  W(1)=W/.695
530  PRINT "THETA =",H,"AUV=",A,"PU=",P,"HW=",W,"NUV=",W(4),"T0=",T0
540  W(6)=0
550  FOR D=1 TO G
560  T=T(D)
570  R=EXP(-W(1)/T)
580  U=0
590  Z=0
600  W(2)=1/(EXP(W(1)/T)-1)
610  !  W(2) IS <M>U
620  !  **  Pu CHANGE WITH TEMP
630  IF T<=275 THEN 660
640  IF F1=1 THEN 660
650  P=P-1  @  F1=1
660  IF P>=0 THEN 760
670  !  **** FINDING M0
680  FOR M=0 TO S-1
690  Y=(SIN(H)/COS(H))^2*M
700  IF Y=INT(Y) THEN 720
710  Y=CEIL(Y)
720  IF P+Y=0 THEN 740
730  NEXT M
740  Q=M
750  GO TO 770
760  Q=0
770  FOR M=Q TO S-1
780  !  ****  CALC OF UPU
790  Y=(SIN(H)/COS(H))^2*M
800  IF Y=INT(Y) THEN 820
810  Y=CEIL(Y)
820  N=Y+P
830  F=Y-(SIN(H)/COS(H))^2*M
840  IF P>=0 THEN 880
850  IF N>=0 THEN 880
860  U(M)=0
870  GO TO 890
880  U(M)=F*A(N-1,M)^2+(1-F)*A(N,M)^2
890  X=(1-R)*R^M*U(M)
900  U=X+U
910  Z=Z+M*X
```

```
 920  NEXT M
 930  !  Z IS <M> PU
 940  Z=Z/U
 950  !  J IS EPU
 960  J=(Z-W(2))*W(1)
 970  !  L IS APU
 980  L=U*EXP(J/T)
 990  Q(D)=TO/(1+TO*W(4)*U)
1000  W(6)=W(6)+(L(D)-Q(D))^2
1010  PRINT "TEMP", "LT-EXP", "LT-CALC", "UPU"
1020  PRINT T(D),L(D),Q(D),U
1030  NEXT D
1040  W(3)=SQR(W(6))/G
1050  PRINT "THE ERROR IS", W(3)
1060  DATA 12
1070  DATA 40,.0114,80,.0114,120,.0114,160,.0114,200,.0108,240,.0103
      260,.0083
1080  DATA 280,.0057,290,.0037,300,.0029,310,.00175,320,.00095
1090  END
```

VITA

Leonard Norman Feuerhelm

Candidate for the Degree of

Doctor of Philosophy

Thesis: OPTICAL PROPERTIES OF Ni^{2+} AND RADIATION DEFECTS IN MgF_2 AND MnF_2

Major Field: Physics

Biographical:

Personal Data: Born in Eldora, Iowa, July 9, 1949, the son of Leonard and Daisy Feuerhelm.

Education: Attended primary school in Albion, Iowa; attended secondary schools in Cedar Rapids, Iowa, and Burlington, Iowa; graduated from Burlington High School in 1967; received Bachelor of Science degree from Oklahoma State University with a major in physics in January, 1971; received Master of Science degree from Oklahoma State University in physics in July, 1973; completed requirements for Doctor of Philosophy degree at Oklahoma State University in December, 1980.

Experience: Graduate Teaching Assistant in the Physics Department at Oklahoma State University (1971-1972); 3-M Company Research Fellow in Physics Department, of Oklahoma State University (1972-1973); Physical Scientist with the United State Government (1973-1976); Instructor of Physics and Math at Oklahoma Christian College (1976-1978); Assistant Professor of Physics at Oklahoma Christian College (1978-1980)